



Master of Science in Applied and Engineering Physics

Constraining New, Heavy, Long-Lived Charged Particles using the IceCube Neutrino Observatory

A First Sensitivity Study to Constrain the Stau Mass Using a Novel
Technique Developed for Neutrino Telescopes

Jan-Henrik Schmidt-Dencker

Experimental Physics with Cosmic Particles
Faculty of Physics
Technische Universität München

15. July 2021

Supervisor:
Prof. Dr. Elisa Resconi

Tutors:
Dr. Christian Haack
Stephan Meighen-Berger

Declaration of Authorship

I hereby declare that the thesis submitted is my own independent work. All direct or indirect sources used are acknowledged as references. I am aware that the thesis in digital form can be examined for the use of unauthorized aid and in order to determine whether the thesis as a whole or parts incorporated in it may be deemed as plagiarism. For the comparison of my work with existing sources I agree that it shall be entered in a database where it shall also remain after examination, to enable comparison with future theses submitted. Further rights of reproduction and usage, however, are not granted here. This paper was not previously presented to another examination board and has not been published.

Eidstattliche Erklärung

Ich versichere an Eides Statt durch meine eigenhändige Unterschrift, dass ich die vorliegende Arbeit selbständig angefertigt habe. Die aus fremden Quellen direkt und indirekt übernommenen Gedanken sind als solche kenntlich gemacht. Ich weiß, dass die Arbeit in digitalisierter Form daraufhin überprüft werden kann, ob unerlaubte Hilfsmittel verwendet wurden und ob es sich – insgesamt oder in Teilen – um ein Plagiat handelt. Zum Vergleich meiner Arbeit mit existierenden Quellen darf sie in eine Datenbank eingestellt werden und nach der Überprüfung zum Vergleich mit künftig eingehenden Arbeiten dort verbleiben. Weitere Vervielfältigungs- und Verwertungsrechte werden dadurch nicht eingeräumt. Die Arbeit wurde weder einer anderen Prüfungsbehörde vorgelegt noch veröffentlicht.

Jan-Henrik Schmidt-Dencker

Ort, Datum

CONTENTS

Abstract	vii
Acknowledgements	ix
1 Introduction	1
2 Beyond the Standard Model: The Stau in Supersymmetry	3
2.1 Supersymmetry	4
2.2 The Stau	6
2.3 Stau searches	10
3 Cosmic Rays and Atmospheric Cascades	11
3.1 Cosmic Rays	13
3.2 Atmospheric Cascades	15
3.3 Multi-Messenger Astronomy	18
4 The IceCube Neutrino Observatory	21
4.1 The Detector	21
4.2 Analyses with IceCube	24
4.3 Event Reconstruction & Topologies	24
4.4 Staus in IceCube	26
5 Particle and Detector Simulation	29
5.1 Stau Flux at Detector Surface	30
5.2 Particles inside the Detector	32
5.3 Event Reconstruction	32
5.4 Background	35
5.5 Event Selection	38
5.6 Calculations	39
6 Findings	43
6.1 Event Reconstruction	43
6.2 Effective Area	46

CONTENTS

6.3 Stau Rates	49
6.4 Stau Mass Limit	51
7 Conclusion	55
8 Outlook and Improvements	57
8.1 Potential of the Analysis	57
8.2 Improved Energy Estimator	59
8.3 Improvements Outside the Analysis	62
A Supplementary Material	65
A.1 MC Samples and Cuts	65
A.2 NLSP Condition and Stau Mass Matrix	65
A.3 Parameters CR Model	66
A.4 Travel Length Simulation in Ice	66
Bibliography	71

ABSTRACT

In this thesis, we explore the capability of neutrino experiments to detect heavy, charged, long-lived Beyond Standard Model particles. For the demonstration of the technique, we perform an example Monte Carlo analysis using the IceCube Neutrino Observatory. There we set limits on the supersymmetric partner of the tau lepton, the stau. To make these limits as model independent as possible, we assume that staus are produced via Drell-Yan interactions between cosmic rays and the atmosphere.

The stau, appears in some models as the next-to-lightest supersymmetric particle. In most cases, this makes it a long-lived particle able to travel macroscopic distances and reach the IceCube detector. When traveling through the detector, the usually heavy staus ($m \gtrsim \mathcal{O}(100)$ GeV) then produce long, dim tracks. Independent of their primary energy, the stau tracks appear as low-energy muons. A potential stau signal would then appear as an excess of minimally ionizing tracks.

The background of our analysis are muons produced in hadronic interactions in the atmosphere and muons from neutrino interactions in the ice. In our study, we calculate an IceCube sensitivity of 62.9 GeV, demonstrating the capability of the analysis to constrain new physics. Reaching the theoretically possible sensitivity of ~ 500 GeV still requires further improvements, some of which are demonstrated in this work.

ACKNOWLEDGEMENTS

First of all, I thank my two supervisors **Christian Haack** and **Stephan Meighen-Berger** for their extensive assistance throughout my entire thesis. I could not have wished for a better team to support me in my efforts than a wise theoretician and an accomplished IceCube statistician. Thank you for always having the time and the patience to help, teach and advise me in every way possible.

Another big thank you goes to **Elisa Resconi** for giving me the opportunity to write this thesis and for leading the group through the -here it comes- pandemic in an exemplary way. Without her support, ambition and care the past year would have been much more difficult to write a master's thesis.

Additionally, I want to thank all members of the **ECP Group** for their cooperativeness and good will. All of you have made it very easy to become part of the group and made me feel welcome from day one.

On a personal remark, I am very grateful to **Laura Winter** for all the emotional support and sympathy over the past year. Thanks to you, my last year was also filled with a lot of joy and many memories that do not involve my master's thesis.

I especially thank **Tim Rieth** who accompanied me from the starting point at the 'T' to the finish line of the 'M'. Since seven years, you fill my life with stimulating discussions and great moments of friendship for which I am truly thankful.

Last, but not least, I thank my parents **Silke** and **Hans Michael** and all of my brothers and sisters for always having my back and being the true north in an ever changing world. Without all of you I would not be the person I am today.

1 | INTRODUCTION

The Standard Model of Particle Physics (SM) provides a self-consistent framework to describe most of the currently known fundamental forces and particles. Numerous observations however, indicate the incompleteness of the Standard Model and create the urge for elaborate extensions. Approaches that incorporate a more complete picture of our universe appear plentiful and long for their exploration. When theories are able to predict a measurable quantity like a new particle or parameter, experiments can be designed to particularly search for the newly postulated physics. Sometimes however, experiments with different purpose are able to engage in the search for new physics as well.

In this thesis, we demonstrate the potential of existing neutrino observatories to constrain physics Beyond the Standard Model (BSM). We make an example for the IceCube neutrino observatory to evaluate the discovery potential of the supersymmetric partner of the tau lepton, the stau, following the theoretical predictions of [1].

We give an introduction to supersymmetry and discuss the parameter space of the stau inside the model. There we explain the circumstances that make the stau detectable in the first place and which features we exploit for our analysis. In this work, we assume that staus are produced in Drell-Yan interactions in cosmic ray (CR) air showers. After the explicit description of the stau production, we go into detail about the nature of air showers. We comment their evolution in the atmosphere and shortly point out the significance of their detection for physics in the context of multi-messenger astronomy.

This is followed by a detailed description of the detector and its working principle. We mention a small selection of analyses carried out with the detector and explain the different event topologies. In this regard, we also discuss the event signature of staus inside the detector.

The next chapter is dedicated to the simulations carried out in this thesis. We start with the details on the stau flux simulation at the detector surface. Thereafter, we state the details on our particle simulation of staus and muons inside the detector as well as the response of the detector to the signal. In addition, we explain the reconstruction methods used and give an overview on the background of our analysis. With the definitions of signal and background, we proceed to the details of our event selection and how it affects the respective distribution. To complete our simulations chapter, we specify the

calculations that make up our signal acceptance and define the χ^2 measures used in the analysis.

After we explained the details of our analysis methods, we present their results using Monte Carlo (MC) simulation data. In this step, we demonstrate the feasibility of this novel approach by showing the sensitivities to constrain the stau mass with the IceCube neutrino observatory. With all of this, we illustrate the relevance of this technique using existing neutrino telescopes.

In the last two chapters, we present our conclusions and give an outlook on the future potential of the analysis. Therefore, we identify potential sources of improvement and assess their impact by illustrating an example. To conclude, we discuss the impact of future neutrino telescopes in order to make the analysis competitive with collider experiments.

2 | BEYOND THE STANDARD MODEL: THE STAU IN SUPERSYMMETRY

The Standard Model of particle physics describes every elementary particle and most of the forces, that we have come across so far. It has been developed over many years and is to this day still the most accurate and precise theory explaining non-gravitational interactions ([2–7]). With a framework of fundamental symmetries and the characterization of interactions it remains a good description for most observations and has been validated by many experiments.

Although no other particles besides those predicted by the SM have yet been discovered, numerous indications suggest BSM physics. Despite its comprehensive contents, the SM lacks explanations for several phenomena. These phenomena include for example gravity, rotation curves of galaxies [8], the distribution of the cosmic microwave background [9] or massive neutrinos [10, 11].

For example, the study of rotation curves from galaxies yields a discrepancy if the gravitational force of the visible mass were to account for the centripetal force alone. In other words, the observed rotation velocity of objects in a stable spiraling galaxy is too high for the visible mass. While there are other theories that for example suggest a modification of Newtonian dynamics (see [12, 13]), an explanation using a higher mass density is favored by many physicists.

From models with higher mass density it follows that the baryonic matter of the SM accounts for only about 5% of the constituents of the universe. This raises questions about the other 95%, not included in the SM. However, also the Hierarchy problem, i.e. the maintenance of mass hierarchy between weak scale, grand unified theory and Planck scale ($M_{weak} \ll M_{GUT}, M_{Planck}$), remains unsolved within the SM. Especially in this regard, the principle of Supersymmetry (SUSY) provides an elegant solution.

This chapter starts with a short introduction to the principle of SUSY and one of its representatives. Explanations are held short and only cover the basics needed with regards to the topic of this thesis (for a review see [14]). The selected model covered is the minimal supersymmetric extension to the Standard Model (MSSM) where some scenarios propose the stau to be a long-lived particle. Another section provides a more detailed view on the particle in question itself, the stau. Besides its basic properties, the production

process and the particles propagation through matter are explained. The final section of this chapter mentions and explores other search attempts for the stau. This includes collider based searches as well as searches for parallel tracks in neutrino telescopes.

2.1 SUPERSYMMETRY

Any model connecting particles and fields with different spin is called supersymmetric. More specific, any theory that is invariant under transformations that connect particles whose spins differ by 1/2 underlies the SUSY principle [15].

SUSY introduces a higher level of symmetry that links fermions and bosons. As a consequence of this, every SM particle has a supersymmetric counterpart of the opposing kind (fermion \rightleftharpoons boson). The supersymmetric partners of fermions are hereby often referred to with an 's' in front whereas the bosons get an Italian ending on 'ino'. All of the SM particles and the main SUSY sparticles can be seen in Figure 2.1.

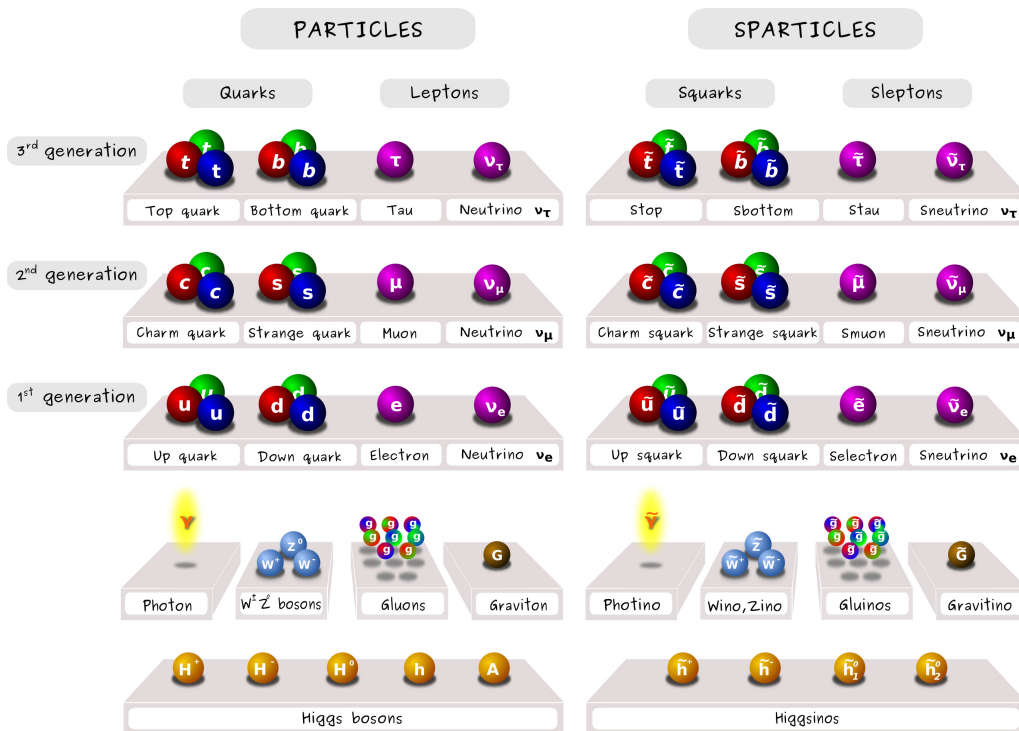


Figure 2.1: The Standard Model particles and their supersymmetric counterparts. [16] Note that this is the depiction of one model using SUSY and that not every model necessarily includes these particle. The focus in this thesis lies on the supersymmetric partner of the tau lepton, displayed in this picture as the second from the top right corner, the stau.

For SUSY to be an exact symmetry of nature, SM particles and their superpartners would be degenerate in mass and would have already been observed [17]. This suggests that

SUSY is a broken symmetry at some mass scale Λ . Up to Λ , the SM is valid and can be seen as a low-energy effective-field theory [14]. The assumed energy range of SUSY breaking has a direct influence on the parameters of the models and can range from 10^3 GeV to 10^{12} GeV [18]. If Λ lies in the higher energy regime, i.e. $>10^{10}$ GeV, the lightest supersymmetric particle (LSP) would be a neutralino. For Λ lower than 10^{10} GeV and a model that extends to include gravity, the LSP is the gravitino [18, 19].

SUSY breaking at higher mass scales ($>10^{10}$ GeV) causes problems at maintaining the gauge hierarchy. Although it is possible with fine tuning of bare parameters, it is regarded to be an unnatural treatment and was meant to be avoided in the first place [14]. The stability of the gauge hierarchy can however be maintained when the breaking is only soft [20]. Origin and fundamentals of the SUSY breaking mechanism remain without an explanation to this day.

Hence, as per the motivation to introduce SUSY, namely for solving the Hierarchy problem, a breaking at TeV scale is favored by many models. One example of this is the MSSM that was initiated by the SUSY SU(5) Grand Unified Theory from Dimopoulos and Georgi [21] but also from Sakai [22].

MSSM As per its name, the MSSM features the smallest possible increase in field content among the SUSY models. Apart from the supersymmetric partners of every SM particle, only the fields of two complex Higgs-doublets are added to the SM (Figure 2.1).

In the Lagrangian, baryon (B) and lepton (L) number violating terms are introduced and would allow processes like proton decays [15]. To compensate for that, an additional symmetry is required, R-Parity. R-parity is formulated as:

$$P_R = (-1)^{3(B-L)+2S}, \quad (2.1)$$

where S is the spin of the particle [23]. This symmetry assigns an even parity to all SM particles and gives an odd R-parity to the supersymmetric partner. When R-parity is conserved, this means two things. One, sparticles are only produced or annihilated in pairs providing the basis for double track motivated searches (section 2.3). The second implication is that decays of superpartners ultimately lead to the production of the LSP [24].

In its most general form, the MSSM is defined by ~ 124 independent physical parameters, mostly due to the soft-supersymmetry-breaking sector [25]. From those, 105 are newly introduced because of the model whereas 18 correspond to SM parameters. The last parameter is a Higgs sector parameter which is analog to the SM Higgs mass [14]. Many of the 105 parameters however, are restricted by observations.

Besides the Hierarchy problem, SUSY theories like the MSSM often provide a partial explanation for the existence of Dark Matter. Through the introduction of R-parity, the decay of the LSP into any SM particle is forbidden making it a stable particle. Usually

a stable LSP with its weakly interacting, massive nature is assumed to be a promising candidate for non-baryonic matter. Even though the LSP of SUSY models cannot solely account for the energy density assigned to Dark Matter, it represents part of the solution. In addition, many SUSY theories have a framework for the gauge coupling unification at very high energies and also accommodate for gravity, whereas the SM is not able to do so. [14, 15] Each and every feature represents a motivation for research in the direction of SUSY theories.

The focus of this thesis lies on the discovery of staus, the supersymmetric partners of the tau lepton (Figure 2.1). They are particularly interesting as in some models they are long-lived particles. Only then is it possible for the stau to travel macroscopic distances and reach a well-shielded neutrino detector. This scenario happens in models where the gravitino is the LSP and the stau is the next-to-lightest supersymmetric particle (NLSP). As the gravitino is the SUSY partner of the graviton and only takes part in gravitational interactions, the decay of the charged stau is suppressed by the scale of supersymmetry breaking, making it a long-lived particle [18, 19]. Hence, the emphasis when discussing the stau properties in section 2.2 concentrates on the very models where the stau is the NLSP to the gravitino.

2.2 THE STAU

Models with the gravitino as the LSP, can typically have three different NLSP's dependent on the choice of the parameters. The most popular ones are the neutralino and the stau, whereas the sneutrino is less famous because of its very restricted region of parameters [26]. A NLSP is unstable and decays into its SM partner and the gravitino. Despite being unstable, there are scenarios where a NLSP is long-lived and able to travel macroscopic distances. In [26] we find a condition for which the stau is lighter than the neutralino and therefore represents the NLSP. The formula is stated and shortly explained in section A.2.

Many of the details on particle properties can be derived from simulations of the big bang nucleosynthesis (BBN). If the lifetime of a NLSP exceeds the duration of BBN ($\sim 1s$), its decay could have produced energetic particles that dissociate the background nuclei and ultimately affect the primordial abundance of light elements noticeably [27]. In some scenarios the rate of decays is high enough to result in a failure of the primordial nucleosynthesis. Another crucial reaction with the NLSP X^- is



where the X^- forms a bound state and produces 6Li . Depending on today's abundance of 6Li , properties of X^- , in particular its lifetime, can be constrained [28]. Constraints given by an intact BBN mechanism and other sources were studied in [29, 30] and suggest the stau as the favoured NLSP candidate.

Another equivalent but simpler expression as Equation A.1, tells us that the nature of the NLSP is defined by the relation between the universal gaugino mass m_0 and the universal scalar mass $m_{1/2}$. For $m_0 \ll m_{1/2}$ the stau is lighter than the neutralino (stau mass $m_{\tilde{\tau}} \simeq 0.387m_{1/2}$) [27]. The same reference supposes a stau lifetime between $1 \times 10^3 s$ and $5 \times 10^3 s$ from catalyzed BBN constraints in order for the mechanism to work but not be too strong to spoil the result.

In the first place, the other sleptons, selectron and smuon, could be the NLSP as well. However, because of mixing effects in the mass matrix related to $\tan \beta$ the stau is the lightest among the three generations [26]. It is also the $\tan \beta$ mixing together with the gaugino-higgs mixing that determines the overall polarization of the stau (L left or R ight) [31].

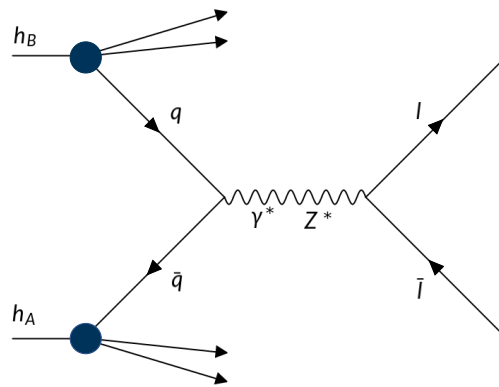


Figure 2.2: Feynman diagram of a Drell-Yan process on the production of staus in our analysis. In our case, the two outgoing leptons are a pair of staus $\tilde{\tau}$.

PRODUCTION As the stau production via strong interaction processes is already well covered by collider experiments, we concentrate on the production by the Drell-Yan process. Figure 2.2 shows a Feynman diagram which represents an example of such a Drell-Yan process. A quark and an anti-quark of two hadrons annihilate to produce a lepton and its anti-partner [32]. Also pairs of sleptons like the stau can be produced through this process. Additionally, the assumption of a stau production solely from Drell-Yan processes has two main advantages [33].

- Drell-Yan processes only depend on two parameters of the MSSM, namely the stau

mass $m_{\tilde{\tau}}$ and the stau mixing angle $\theta_{\tilde{\tau}}$ respectively. For the latter we use the one defined by the MSSM model in MadGraph [34].

- Due to the independence of many MSSM parameters and its omnipresence in nature, a definite discovery potential can be determined and with that also an exclusion limit on $m_{\tilde{\tau}}$.

A depiction of the interaction cross section of the process with respect to the stau mass is shown in Figure 2.3. The plot contains data generated by MadGraph [34] for the $pp \rightarrow Z^*, \gamma^* \rightarrow \tilde{\tau}^+ \tilde{\tau}^-$ interaction at two different beam energies. We see that higher proton beam energies lead to a higher overall cross section for the stau production. Additionally, we see an exponential decrease for the production of stau pairs when incrementing the assumed stau mass.

Unlike the tree-level cross sections for proton beam collisions shown in Figure 2.3, our analysis assumes staus to be produced by cosmic rays (protons) hitting the atmosphere (air). This difference between proton-proton and proton air collisions creates the need for a correction of the cross sections. In order to generalize the MadGraph data to the proton-air collision cross section, we use the Glauber formalism [35, 36].

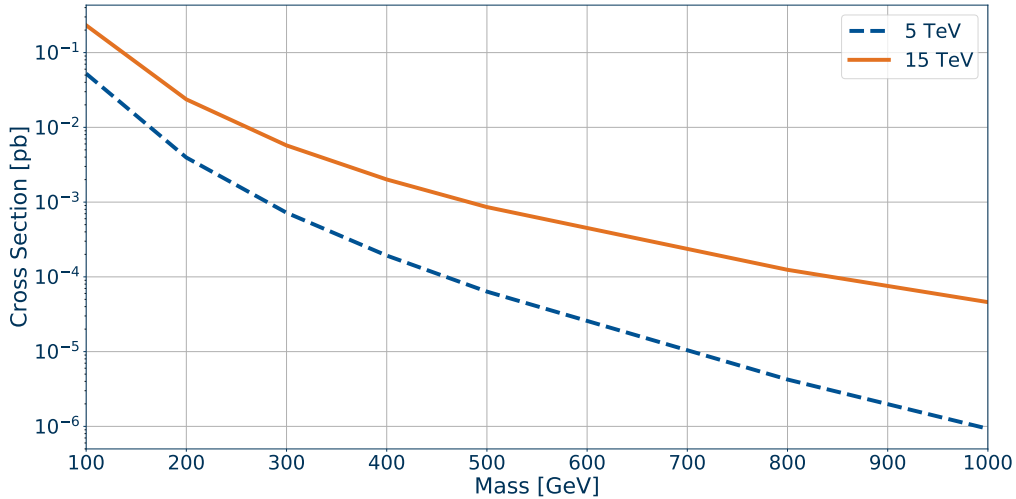


Figure 2.3: Stau mass dependence of the cross section for the stau production at proton-proton collisions. Displayed is the data of two different beam energies simulated by MadGraph [34]. Note, that the displayed cross sections are tree-level data. For higher orders and corrections see [37].

PROPAGATION When passing through matter the stau loses energy due to ionization and radiation processes. A formulation of the average energy loss of a charged particle traveling a distance X [g/cm^2] is given through

$$-\frac{dE}{dX} = a(E) + b(E)E, \quad (2.3)$$

where a and b depend on the traversed material and the particle passing through. Hereby $a(E)$ represents the energy loss due to ionization and $b(E)$ accounts for radiation or stochastic losses. In general, staus traversing matter behave similar to muons. The only significant difference is the mass of the particles. Whereas muons have a mass of 105 MeV the stau mass is assumed to be in the hundreds of GeV or even TeV range. Ionization losses are independent of the mass, meaning that $a_\mu(E) \approx a_\tau(E)$. Stochastic loss mechanisms, namely pair production, bremsstrahlung and photonuclear interactions, depend on the mass of the particle. Thereby the differential cross sections of pair production and photonuclear interactions scale linearly with the mass, whereas for bremsstrahlung we observe a scaling with the mass squared [38].

For our analysis, we thus approximate that $b_\mu(E)m_\mu \approx b_\tau(E)m_\tau$ [39]. Scaling the mass dependent stochastic energy losses by a stau mass of 100 GeV results in the energy loss behavior from Figure 2.4. This plot demonstrates the difference in energy loss resulting from the suppression of stochastic processes by the stau mass. Even in regions where the muon energy loss is strongly dominated by stochastic processes, the stau follows the ionization losses of the muon. Assuming an even higher stau mass than 100 GeV, results in a higher suppression of the stochastic losses. The curve would thus follow the muons' ionization losses even more closely.

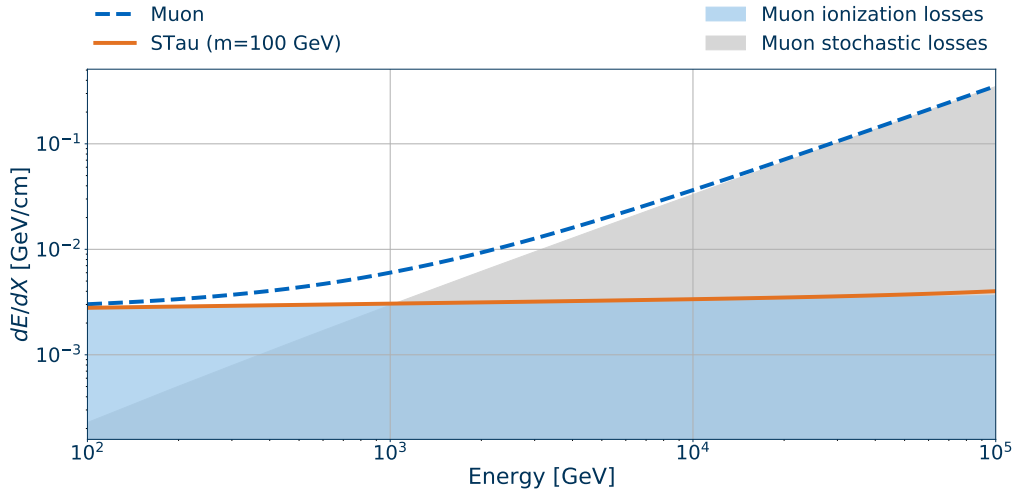


Figure 2.4: Comparison between the energy loss of a stau and a muon in ice, using Equation 2.3 and [40] for values of a and b .

2.3 STAU SEARCHES

Many previous efforts towards finding hints of SUSY have utilized the properties of the stau as the NLSP. Though the gravitino is assumed to be a stable particle, its large mass and its charge have made the stau a more convenient target. In the following, we explain the two essential types of searches that are sensitive to stau signatures resulting from those properties with the same goal as our analysis.

COLLIDER SEARCHES Collider experiments like the LHC use proton-proton collisions to look for BSM particle signatures. Thereby the ionization energy loss (Figure 2.4) and time of flight related properties that are influenced by the significantly higher mass of the slepton work as a signal for the analysis [41]. With the cross sections from Figure 2.3, one is able to calculate the expected amount of produced staus.

For that the presence is directly linked to the mass of the stau, an absence of stau signatures thus excludes a region of possible stau masses. As of the nature of the cross section dependence, lower masses typically yield a higher cross section since less energy is required for their production. Hence, the absence of signatures gives a lower limit on the stau mass. The current limit set by the LHC using the ATLAS detector is 430 GeV [41] at 95% confidence level.

DOUBLE TRACK SEARCHES In contrast to the collider based searches, this approach uses existing large scale neutrino telescopes, operating on the principle of Cherenkov light detection (more detailed description in section 4.1). The staus in this analysis are usually produced in the earth and lead to so called 'up-going' double tracks.

Double track searches exploit the characteristics of conserved R-parity (section 2.1) to generate sleptons in pairs. A large boosting of the stau pair leads to a very small angle between the sparticles. This on the other hand, causes two separated, almost parallel tracks. The separation at the detector depends on the boosting angle and the distance between interaction vertex and the detector.

The boosting factor and therefore the separation is defined by the properties of the incident particles. The higher their energy, the smaller the angle and the separation of the staus at detector level. In SM processes only few interactions result in parallel tracks of muons which makes the detection of an excess of parallel tracks a distinctive signature for BSM physics [18, 42].

Due to the strong boosting, stau track separations are low, even for large distances to the detector. Specifically for IceCube, most of the tracks are separated by less than ~ 50 m [43]. However to resolve double tracks in IceCube, separations of more than ~ 130 m are required [44]. This results in the omission of the majority of the signal.

3 | COSMIC RAYS AND ATMOSPHERIC CASCADES

From the first indication to our current state of knowledge, it has been a long-winded path for Cosmic Rays (CRs). After Victor Hess discovered increasing ionization losses when rising to the sky in a balloon in 1912 [45], speculation began over the nature of the cause. It started disputes from leading physicists all over the world arguing whether particles or radiation are responsible for this phenomenon. During that time, not many particles were known and Hess' findings encouraged the research towards a completely new field. The efforts towards CR research yielded the discovery of unknown particles and formed into what we now recognize as Multi-Messenger Astronomy.

Today we know, that the earth's atmosphere is exposed to radiation and particles originating from all over the universe. The term CR is hereby still not used distinctively and sometimes relates to particles only, while another time it includes radiation as well. We will however, use the expression only as the plurality of energetic particles hitting the atmosphere.

Over a broad range of the energy spectrum, CRs and their composition are well characterized by experiments. Only for the highest energies, experimental data drifts apart and is no longer in agreement. This produces an ambiguity about the nature of the CR acceleration in that energy region and its apparent cut-off.

It is assumed that most particles originate from outside our solar system, but still within our galaxy [46]. The source of CRs becomes particularly interesting when analyzing the high energy range of the spectrum. No conclusive mechanism is able to explain particle energies up to 10^{20} eV. The motivation is hence high for a precise investigation of the origin of those particles.

This chapter starts by explaining the characteristics of CRs. It provides a description of atmospheric cascades as a result of CR interactions in the atmosphere. Furthermore, we address and explain the origin of the signal and background of this analysis. Finally, we include a short introduction to Multi-Messenger Astronomy and emphasize its importance for future discoveries.

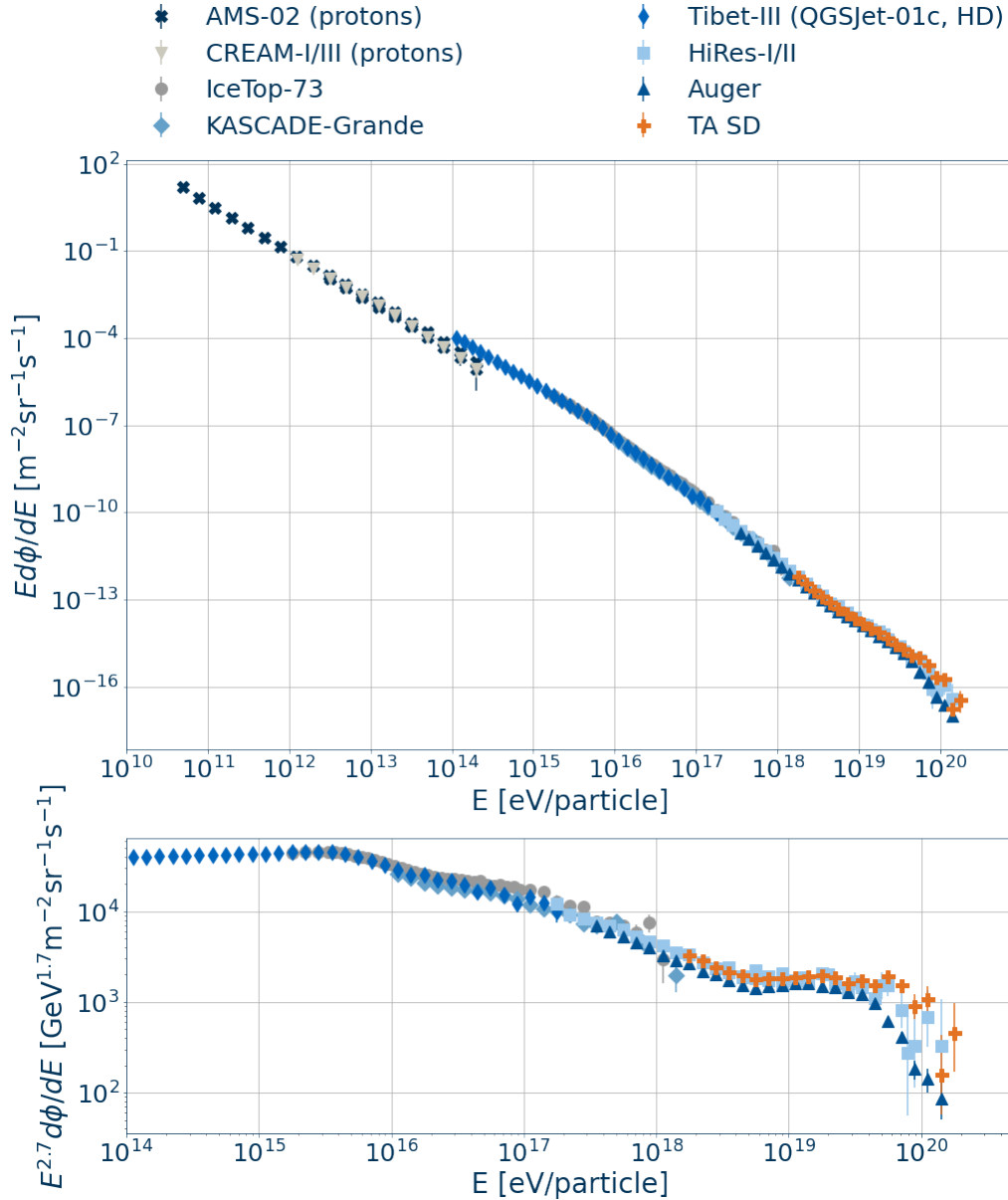


Figure 3.1: Two different representations of the Cosmic Ray spectrum proportional to the energy of the incident particle. The plot on the top includes proton-only measurements for the range below 100 TeV, whereas the bottom plot is restricted to all-particle measurements. In the first graph, the flux is multiplied by the particles energy, which is a common way to depict the event rates, as energy measurements usually have a precision δE , proportional to the energy [46]. In order to enhance the features of the spectrum the flux is usually multiplied by the energy to a higher order (here 2.7). The representation of that is shown in the second graph. Data was taken from [47–54]

3.1 COSMIC RAYS

Approximately 1000 particles per square meter and second hit the atmosphere with $\sim 90\%$ of those CRs being protons [46]. Their arrival direction spreads around the earth almost isotropically, due to astrophysical magnetic fields [55].

Figure 3.1 includes two standard ways to view the flux of CRs proportional to the energy of the incident particle. The top depicts the raw flux data multiplied by the energy from different experiments over the whole energy range. In the bottom graph the data is multiplied by a factor of $E^{2.7}$ and focuses on energies above 10^{14} eV. We see that the multiplication by $E^{2.7}$ in the bottom plot enhances the famous features, 'knee' (10^{15} eV - 10^{16} eV), 'ankle' (10^{18} eV - 10^{19} eV) and the sudden cut-off, of the CR flux.

One way to model the spectrum is represented by building the sum over all individual spectra that contribute to the CR flux. The behavior of the different nucleus species i is modeled by a power law spectrum with $\gamma_{i,j}$ that cuts off exponentially at a characteristic rigidity $R_{c,j}$ [56]. Through the introduction of different origins j for the populations, including an unknown source of high energy protons, it is possible to explain almost every feature with the rigidity (R Equation 3.2) of the particle species. The all-particle spectrum is then given by

$$\Phi_i(E) = \sum_{j=1}^3 a_{i,j} E^{-\gamma_{i,j}} \cdot \exp\left(-\frac{E}{Z_i R_{c,j}}\right), \quad (3.1)$$

where Z_i represents the electric charge and $a_{i,j}$ are the normalization constants. A table on the specific parameters used in the model is found in section A.3.

KNEE Around 4 PeV, the energy spectrum steepens and forms the so called 'knee'. Supported by models and data, the knee marks the onset of cut-off energies for the individual elements in the galactic CR component [57]. Assuming that the elements descend from Supernova Remnants and were accelerated by the shock front, the acceleration mechanism reaches its limit close to the knee [46]. The reason for a thinning out instead of a simple drop of the CR flux is the different cut-off energies of the elements and species accounted for in Equation 3.1.

In the acceleration process the maximum energy is related to the electric charge Z of the particle. Because of this, Peters proposed that the composition of the CR spectrum would change above the knee and held the magnetic rigidity R responsible:

$$R := \frac{pc}{Ze} \approx \frac{E}{Ze}, \quad (3.2)$$

with E , the total energy of the nucleus, over the charge Ze [58]. Particles with higher charge can attain higher energies in the acceleration and will thus be cut-off later. The

CR composition then tends towards heavier nuclei and is no longer dominated by protons as lighter elements die away first [59]. Following through with this explanation, we get to a point where also the element with the highest rigidity of galactic origin reaches its cut-off energy. This point is believed to be the ankle of the spectrum.

ANKLE The ankle marks the point of the spectrum where the original power law (~ 2.7) applies again and the curve flattens. In contrast to the well-established theory to the knee of the spectrum, the region from ankle to the ultimate cut-off still underlies speculation. Reason for this is mainly the low statistics arising from a combination of low flux and few experiments.

Although the onset energy of the ankle feature is well-established, the discrepancy in the data thereafter allows for two possible explanations related to the nature of the cut-off. [60]

- In a scenario where the ultra high energy region of the CR spectrum corresponds to an almost pure proton composition, the ankle can be interpreted as e^+e^- pair production losses of the CMB. Hereby the cut-off is consistent with the one described by the Greisen-Zatsepin-Kuzmin(GZK) effect.
- The second scenario relates the ankle to the transition from galactic to extra galactic CRs. Hereby the ultimate cut-off is assumed to be of a maximum energy nature.

CUT-OFF The explanation for the cut-off of the CR spectrum and the background of the ankle are entangled. In a maximum energy scenario the extra galactic particles are accelerated to reach the highest energy possible in their astrophysical environments [46, 61]. Hereby the ankle is viewed as the onset of the remaining extra galactic CR component.

Another explanation was provided by Greisen [62], Zatsepin and Kuzmin [63]. Photons from the cosmic microwave background make the Universe opaque to high energy protons. The first resonance of this mechanism appears for a proton energy of ~ 50 EeV being close to the observed cut-off by experimental data. This mechanism is called the GZK effect and is based on the assumption that the ultra high energy part of the CR spectrum is dominated by protons [55].

The available data on the two eventualities is inconsistent. Whereas data from TA SD is compatible with a pure proton composition of the CR flux, the Auger data suggests a bias towards heavier nuclei. Hence, TA SD [64] supports the prospect of seeing the GZK effect, while Auger data [65] emphasizes a maximum energy scenario [60].

A combined analysis of the two data sets in [66] was able to explain some of the discrepancies by comparing the MC simulation procedures. Both experiments used different hadronic interaction models and different fluorescence models for their simulations. Although this explains why both experiments claim a different composition of the CRs, the varying behavior of the cut-off remains unclear.

A closer look on the anisotropy of the CR spectrum can yield a decision between the two

possibilities. The effects in question, influence the level of anisotropy in the high energy CR sky. An observation of a highly isotropic CR-sky would conflict with a pure proton composition. This combination is only feasible when assuming strong galactic and extra galactic magnetic fields [60]. Otherwise the maximum energy scenario is favored.

As the CR spectrum spans over a large energy range (~ 1 GeV to 100 EeV), several different experiments and techniques are needed to cover for it. Notice, that the data in [Figure 3.1](#) for the energy range below 10^{14} eV shows measurements of proton CRs only.

Below a few hundred TeV data is gathered by the Alpha Magnetic Spectrometer (AMS) at the International Space Station [47] and the balloon-borne experiment CREAM at the top of the atmosphere [48]. Protons are hereby measured directly before they have a chance to interact with the particles in the atmosphere. Other experiments like Pierre-Auger [53] follow a ground based approach to register air showers from atmospheric cascades (see [section 3.2](#)).

The different approaches become necessary for the combinations of flux and energy of the particle. For low energy particles, the triggered air shower is almost entirely absorbed by the atmosphere on its way to the surface. Ground based experiments would not be able to measure enough secondary particles for an accurate energy reconstruction and are thus unsuitable. The high flux of low energy CRs however, enables a smaller detector size and makes space based approaches feasible.

In contrast to low energy CRs, the flux for higher energy particles steeply decreases. While at approximately 100 GeV we get 1 particle/m²/s, at energies of some PeV (10^{15} eV) we merely get 1 particle/m²/a. At even higher energies ~ 10 EeV (10^{19} eV) the flux comes down to 1 particle/km²/a, creating the necessity for large scale telescopes.

These large telescopes measure the light emerging from so called air showers and the fluorescence light caused by the secondary particles produced in the shower. Air showers evolve as a cascade of particles in the atmosphere triggered by an initial primary CR interaction. Through the different populations of arriving particles and their energies the experiment infers the properties of the primary. A more detailed view on air showers or atmospheric cascades is given in the following section.

3.2 ATMOSPHERIC CASCADES

When a CR, referred to as the primary, hits the particles in the atmosphere, it initiates a chain reaction and disperses its energy into the creation of other particles, called secondaries. Primaries, heavier than protons, may also decay into other particles which then trigger an air shower. An exemplary sketch of the arising particle cascade caused by a primary CR can be seen in [Figure 3.2](#).

Depending on nature and energy of the primary, the air shower takes on different shapes

A first conceivable approach of modeling the individual particles might be a MC simulation. This involves the propagation of each individual secondary particle and the cascades triggered by their interactions. Such an effort is done and provided by CORSIKA [69]. Simulating each and every particle of an air shower is however computationally expensive and time consuming. Hence, despite the higher accuracy of MC approaches, sometimes a more practical treatment by a set of coupled cascade equations is sufficient.

Coupled cascade equations handle the treatment of air showers by describing the average particle fluxes at different levels of the atmosphere [46]. This approach offers a computationally less exhausting and fast way of simulating the full cascade down to the detector level. Furthermore, the calculation within seconds enables the study of particle populations at every level being influenced by different parameters of the particles, for example the lifetime.

The downside of using cascade equations resides in the assumption that all generated particles proceed to the next level. Despite the possibility for secondary particles to escape the shower, they are propagated to the earth. The transverse dispersion of the cascade is thereby currently completely disregarded. So called-3D effects however, are sub-dominant for energies above a few GeV and prove the cascade formalism to be valid above these energies [55].

Additionally note, that calculations of cascade equations are not statistical and do not account for any fluctuations. For the modeling of individual particle showers this approach is impractical as the equations only provide predictions concerning average particle fluxes. As we are not interested in exact shower topologies, our analysis benefits from an application of matrix cascade equations over elaborate MC simulations.

STAU PRODUCTION The Feynman diagram from Figure 2.2 shows the production mechanism of the stau. Given that the incident particles provide enough energy to produce a pair of staus, the Drell-Yan process can happen at any depth in the atmosphere. Any interaction between a primary or secondary hadron h of an air shower with a nucleon in the atmosphere has the potential to result in the production of staus. This potential is realized in the probability $P_{\tilde{\tau}}^h$,

$$P_{\tilde{\tau}}^h(E) \approx \frac{A\sigma_{\tilde{\tau}}^{h,nucleon}}{\sigma_{total}^{h,air}}. \quad (3.3)$$

The probability consists of the relation between the cross section for stau generation $\sigma_{\tilde{\tau}}^{h,nucleon}$ and the total cross section of h with air $\sigma_{total}^{h,air}$. A hereby represents the average number of nucleons in a nucleus of air and is set to 14.6 for our calculations.

Although it is possible for the stau to be produced in every depth, it is more likely to emerge from a primary interaction. Furthermore, we assume that most of the energy of the primary is converted into the production of the stau [38]. One possible way for

the discrimination between signal and background could thus be a lack of secondary particles.

BACKGROUND When using the atmosphere as an ultra high energy collider, a multitude of particles is produced besides the ones desired. An atmospheric cascade induces a lot of background for experiments not particularly interested in the primary or the shower. Especially neutrino telescopes like the IceCube Neutrino Observatory, deal with a lot of background from the atmosphere.

In [Figure 3.2](#) we see a small variety of the produced particles by atmospheric air showers. The most dominant background for neutrino telescopes is represented by muons and neutrinos of all flavors. As per their origin they are usually referred to as atmospheric muons and atmospheric neutrinos.

In our case, the stau signal inside the detector ([section 4.4](#)) is similar to the signature of muons. This makes muons from atmospheric showers and from atmospheric muon neutrino interactions our main background. More details on the background are given in [section 5.4](#).

3.3 MULTI-MESSENGER ASTRONOMY

Although the discovery of CRs initiated important discoveries, the ultra high energy of some and their origin still remains a mystery. No object in our galaxy has yet been observed to produce particles of energies on the order of EeV. The search for their origin however, becomes difficult when their way through the universe is influenced by magnetic fields. In this case, their arrival direction at the top of the earth's atmosphere does not point back directly to their origin. Thus, a stand-alone search only with CR telescopes, makes a discovery of potential sources difficult.

However, the assumption that environments with an acceleration power like this generate auxiliary particles allows further investigations of the CR sky. [Figure 3.3](#) displays this scenario with two other messengers next to CRs (red), namely Gamma rays (blue) and neutrinos (green).¹

The sketch illustrates the deflection of CRs on their way to the earth. In contrast to that, Gamma rays and neutrinos take a more direct path. Similar to CRs, Gamma rays produce air showers as well. The extension and population of the shower thereby indicates whether it was caused by a Gamma ray or a CR. However, even if the directional information of the incident Gamma could be reconstructed perfectly, many Gamma rays will be absorbed while traveling through the universe.

This emphasizes the potential of the third messenger, the neutrino. Due to its small

¹Note that gravitational waves are also considered to carry information about these environments but will not be explained in more detail.

cross section the neutrino travels a long way without interacting. Its charge-less nature preserves it from deflections due to magnetic fields and through the small undetermined mass it is also insensitive to large energy densities. Many experiments thus grasp on the opportunity to search for high energy neutrinos in order to gather their robust directional information pointing back to their source. An explanation on the working principle of the neutrino telescope used in this thesis is given in the next chapter 4.

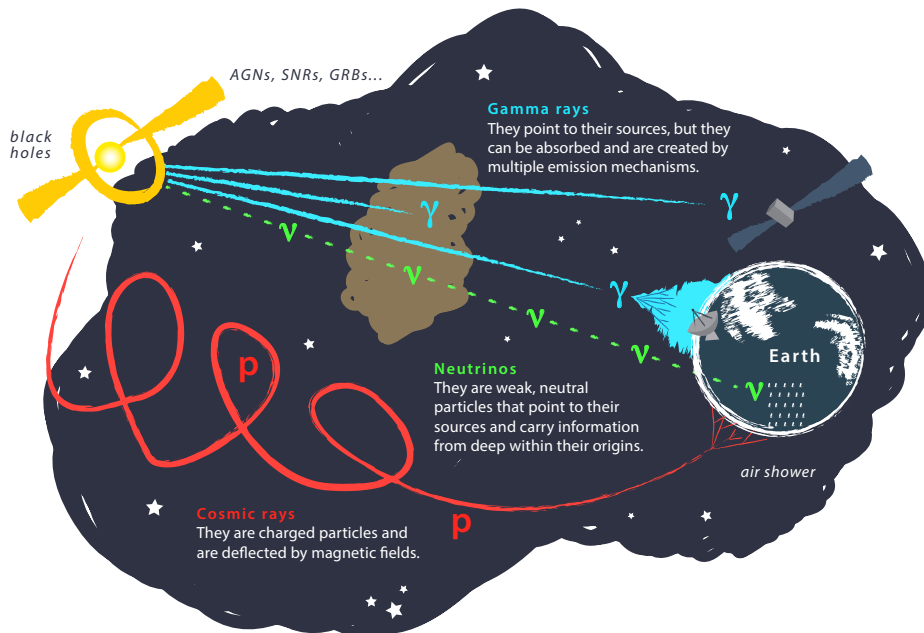


Figure 3.3: Multi-Messenger Astronomy [70]

4 | THE ICECUBE NEUTRINO OBSERVATORY

The idea of having a large volume neutrino telescope arises from the motivation to detect very high energy neutrinos with low flux. Results of previous smaller experiments drove the notion for a telescope with a target material of one cubic kilometer. Experimental studies from Baikal [71], AMANDA [72] and ANTARES [73] proved the concept of a setup in water, solid or liquid, to analyze high energy neutrino events. However, similar to the high energy CRs in Figure 3.1, high energy neutrinos from astrophysical sources have a very low flux [74]. Thus, in order to detect the weakly interacting neutrinos large scale telescopes are needed.

High energy neutrinos are of particular interest because their sources are identical with the origin for high energy CRs [75, 76]. In contrast to other particles, neutrinos interact only weakly with matter so that their path is not affected through mechanisms we know of. Their reconstructed direction can thus point us towards astrophysical sources emitting high energy particles. However, their low interaction probability and lack of charge that make them travel long distances without being deflected also make them hard to detect.

This chapter addresses the detector used in the analysis, the IceCube Neutrino Observatory (IceCube). An in-depth description of the detector is provided by [77]. In addition to the working principle of the detector, we explain the different event topologies observed by IceCube. As a conclusion to this chapter, we describe the behavior of the stau inside IceCube and show a typical event view for our signal.

4.1 THE DETECTOR

IceCube is a neutrino telescope on cubic kilometer scale in the ice of Antarctica. The measurement principle is the detection of Cherenkov light (see Cherenkov Light). Cherenkov photons are registered by photo multiplier tubes (PMTs) which are embedded in digital optical modules (see Digital Optical Module (DOM)). Conjoined with the spacial information of the DOMs, the data is used to reconstruct the properties of the events happening in the detector. These properties include for example the topology, energy and the direction of the event.

DIGITAL OPTICAL MODULE (DOM) A DOM is the fundamental source of data acquisition for the IceCube detector. It mainly consists of a downward-facing 10 inch PMT, a light-emitting-diode (LED) Flasher Board and a Main Board enclosed in a glass sphere [77]. Via cable the DOMs are connected to the research facility located at the surface of the ice. Over this connection the timestamped and pre-processed signals are transferred for further processing [77].

CHERENKOV LIGHT Any charged particle traveling through a material faster than the phase velocity of light produces Cherenkov photons. This phenomenon was first described accurately by Cherenkov in 1937 [78]. He found a relation between the opening angle θ of the light cone, the particle's velocity v and the refractive index of the material n :

$$\cos(\theta) = \frac{1}{\beta n}, \quad (4.1)$$

where $\beta = v/c$. An extensive part on the theoretical description and explanation was given by Frank and Tamm [79].

The wavelengths of the emerging photons are distributed over the whole spectrum of visible light. Their peak, however, lies in the blue regime at about 420 nm [80]. Despite Cherenkov radiation being less relevant for the energy loss in a material, it still is the dominant source for radiation in the visible region [81]. This property is hence used for the detection of high energetic charged particles passing through matter.

In order to detect the Cherenkov photons more easily and cover large volumes, the choice of a suitable material is essential. Water and ice have proven to be beneficial, especially regarding the multiplicity of natural occurrences. Namely for large detector volumes, the use of a naturally existing target and Cherenkov medium is necessary. The long absorption length over a broad volume of ice (see [82]) and the infrastructure at Antarctica make the south pole a well suited location for a neutrino telescope.

Since neutrinos are neutral particles and interact over the weak force, IceCube is only able to measure secondary particles emerging from a neutrino interaction. It is the charged secondaries, which radiate Cherenkov light and are thus registered by the detector. However, due to the low interaction cross section of neutrinos ($\sim 10^{-38}$ cm²/GeV [83, 84]) and the power law spectrum for the neutrino flux, a detection of measurable secondaries induced by high energy neutrinos is challenging. To compensate both cross section and flux, neutrino telescopes ought to have a large scale instrumentation of materials, such as the cubic kilometer of volume for IceCube.

The IceCube detector has essentially four main features. There is the In-Ice array, which includes DeepCore as a second feature and then there are IceTop and the IceCube Lab (ICL). A schematic of those including the precursor AMANDA is pictured in Figure 4.1.

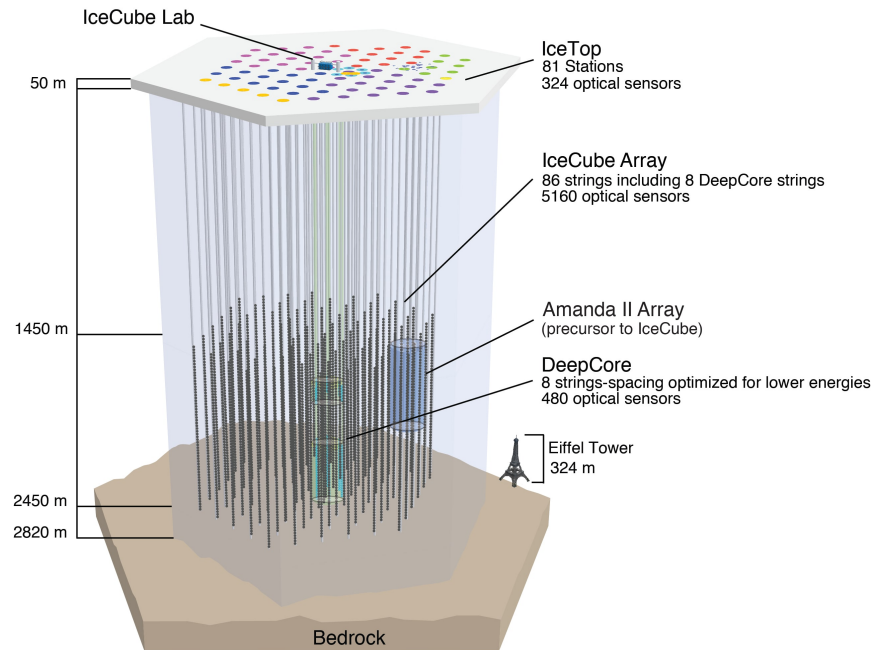


Figure 4.1: Schematic representation of the IceCube Neutrino Observatory at the South Pole including a depiction of the precursor AMANDA

Most relevant for the following analysis is the In-Ice array. The array has 5160 DOMs distributed on to 86 strings. 78 of which are evenly spaced in a hexagonal shape with separations of 125 m. Every string holds 60 DOMs in 17 m distance and is installed vertically in the ice from 1450 m up to 2450 m underneath the surface.

The other eight strings build DeepCore. This subset has a more compact coverage of the ice and has string spacings between 41 m to 105m. On each string, the 50 DOMs on the bottom are separated by 7 m and range from 2450 to 2100 m below the surface. The other ten DOMs are spaced 10 m apart and go up to 2000 m. With the more dense spacing between strings and DOMs, DeepCore is constructed to detect and resolve neutrinos with much lower energies. The design is thereby optimized for energies between 10 GeV and 100 GeV [77].

IceTop is a cosmic air shower array located at the surface. 162 ice-filled tanks are instrumented with PMTs to detect the Cherenkov radiation from particles of air shower events. They are sampled in 81 stations, covering approximately the same grid of the In-Ice array.

4.2 ANALYSES WITH ICECUBE

The ultimate goal of IceCube is the detection of high energy neutrinos from astrophysical origin. This search is linked to the discovery of their sources as we currently lack explanations for the high energy of those particles. Efforts towards finding high energy neutrino sources are published as 'Point Source Searches' [85].

The huge volume in the ice overlooked by PMTs however, opens many more possibilities for different kinds of research. Right from the beginning, the detector was also used to study for example neutrino oscillations [86] and search for supernovae [87], Dark Matter [88], magnetic monopoles [89] and other exotic particles .

Many other complementary studies target the understanding of in-ice effects concerning photon propagation as well as background source estimations (e.g. [90, 91]). These are of particular interest when estimating the systematic uncertainties of the detector. For this regard, the modeling of ice properties is still the object of ongoing research within the IceCube collaboration and undergoes constant improvement [92].

4.3 EVENT RECONSTRUCTION & TOPOLOGIES

Depending on the interaction channel and neutrino flavor the nature of the event inside the detector varies. In general, IceCube differentiates between two basic topologies of signal: tracks and cascades.

CASCADE This event signature is characteristic for charged-current interactions involving ν_e and ν_τ and for all neutral-current interactions. The Cherenkov light seen by the detector comes almost solely from electromagnetic and hadronic showers in the ice.

In the charged-current case of ν_e , electromagnetic showers from the outgoing electron account for the majority of the deposited energy. Alongside electromagnetic showers, charged-current interactions trigger hadronic particle showers as well. In comparison to electromagnetic showers, hadronic showers show a reduced Cherenkov light yield. Due to the formation of more neutral and heavier particles only a fraction of their energy is converted into light-producing particles ($\sim 80\%$ Cherenkov photon yield per GeV [93]). In an average total the charged-current reaction deposits more than 90% of the ν_e 's energy inside the detector [94]. For the inference of the initial neutrino properties, a high energy conversion is very valuable.

While charged-current interactions produce both types of shower inside the detector, neutral-current interactions initiate hadronic showers only. We know that the hadronic shower per se deposits less energy already, but in case of a neutral current interaction most of the energy escapes the detector with the scattered neutrino. On average, only roughly a third of the initial neutrino energy is deposited inside the IceCube detector [94].

Energy reconstruction for cascade like events is much easier than for track events, especially if the whole event is contained inside the detector volume. Namely in this case, a calorimetric approach is applicable and simplifies the energy estimation. The energy deposited inside the detector corresponds directly to the energy associated with the type of neutrino interaction. Nevertheless, it is impossible for IceCube to resolve the differences between neutral- and charged-current cascade events. Hence, every energy reconstruction estimate represents a lower limit on the incident neutrino energy.

In addition to the ν_e charged-current and the all flavor neutral-current interactions, there is another slightly different cascade event type. The charged-current interaction of the ν_τ can produce what is often referred to as a 'double bang'. Hereby the first interaction and the decay of the produced τ cause well separated cascades joined by a track. Whereas IceCube is not able to resolve the very localized cascade event showers (length ~ 10 m [94]), it is able to resolve the separation of the double bang if the energy is high enough.

Another possibility of the ν_τ interaction is a cascade followed by a track. This happens when the interaction causes a first cascade and the τ decays into a muon. Both features of the ν_τ 's charged-current interaction make it possible to look for them specifically.

TRACKS Compared to cascade events, the energy reconstruction of tracks is more complicated. Along its way through the ice, any charged particle produces a track of Cherenkov light. In IceCube, mostly muons are expected to traverse the detector and leave a track like signal. Their origin could be a charged-current interaction of ν_μ but also an air shower in the atmosphere.

Muons with low energies ($\lesssim 300$ GeV see [section A.4](#)) have a travel length shorter than the extent of the detector. Hence, when generated within the detector volume, they will deposit all their energy inside. This makes it easy to estimate their initial energy with a calorimetric approach.

Above this energy, however, the muon track will not be fully contained inside the volume of the detector. In this case, the energy reconstruction has to rely on the differential energy loss rate, i.e. the energy lost in each loss process of the particle. As only part of the entire muon track leads through the detector, the muons point of origin is unknown. Unless the track does not start inside the detector, it may have traveled a long distance before entering it. On its way, the muon already lost part of its energy. Therefore, the energy reconstruction only provides a lower bound to the energy of the neutrino that presumably caused the interaction.

Besides this, the energy reconstruction from the various loss processes holds a multitude of possibilities. The average energy loss is described by [Equation 2.3](#) and involves ionization and stochastic losses. For high muon energies ($\gtrsim 1$ TeV), the energy loss is dominated by stochastic processes (for example bremsstrahlung, pair production [Figure 2.4](#)). The average energy loss rate increases approximately linearly but follows no

consistent pattern as of the nature of the loss processes. Muons with the same energy undergo different stochastic processes throughout their way inside the ice and will leave different energy loss patterns in the detector. [94, 95]

4.4 STAUS IN ICECUBE

When a stau is generated in a CR air shower via the Drell-Yan process described in section 2.2 it encounters continuous energy loss. As for muons, Equation 2.3 describes the energy loss and differentiates between losses of stochastic nature and losses due to ionization. Because of its large mass, stochastic processes are highly suppressed during the propagation of the stau. Hence, the main part of energy loss is thus due to ionization.

Figure 2.4 shows the difference between the energy loss of a muon and a stau. Throughout the plotted range, the energy loss of the stau stays close to the ionization losses of the muon. While stochastic losses start to dominate the energy losses of muons, the stau's losses still compare to a low energy muon.

When comparing the resulting energy deposition of the two particles in Figure 4.2, the effect on the difference in the particle's energy loss becomes evident. We see a steady linear increase until the energy where muon and stau are able to travel a longer distance than the extent of the detector (~ 280 GeV and 310 GeV respectively, see Figure A.1). As soon as this point is reached, the energy deposition drifts apart.

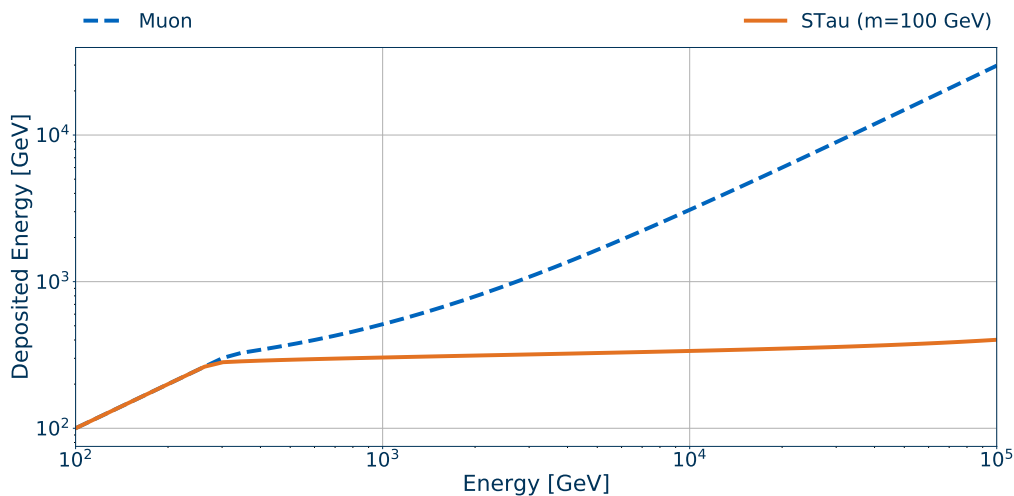


Figure 4.2: Energy deposition inside the detector of a muon and a 100 GeV stau. With the data of the energy loss in Figure 2.4, we calculate the deposition of the particle when traversing the detector (1 km of ice).

According to Figure 4.2, any stau above ~ 280 GeV leaves approximately the same energy inside the detector independent of its initial energy. The energy reconstruction of IceCube will therefore recognize any stau as a low energy muon.

This behavior is illustrated by the event view of a MC stau event in Figure 4.3. There we show an example of a stau track in the IceCube detector. The simulated stau has been initialized with an energy of 23 TeV at a zenith angle of 88.7° . Afterwards, it was reconstructed to an event with 573 GeV and a zenith direction of 88.5° . Altogether, this event view is exemplary of a stau event and emphasizes the working principle of our analysis.

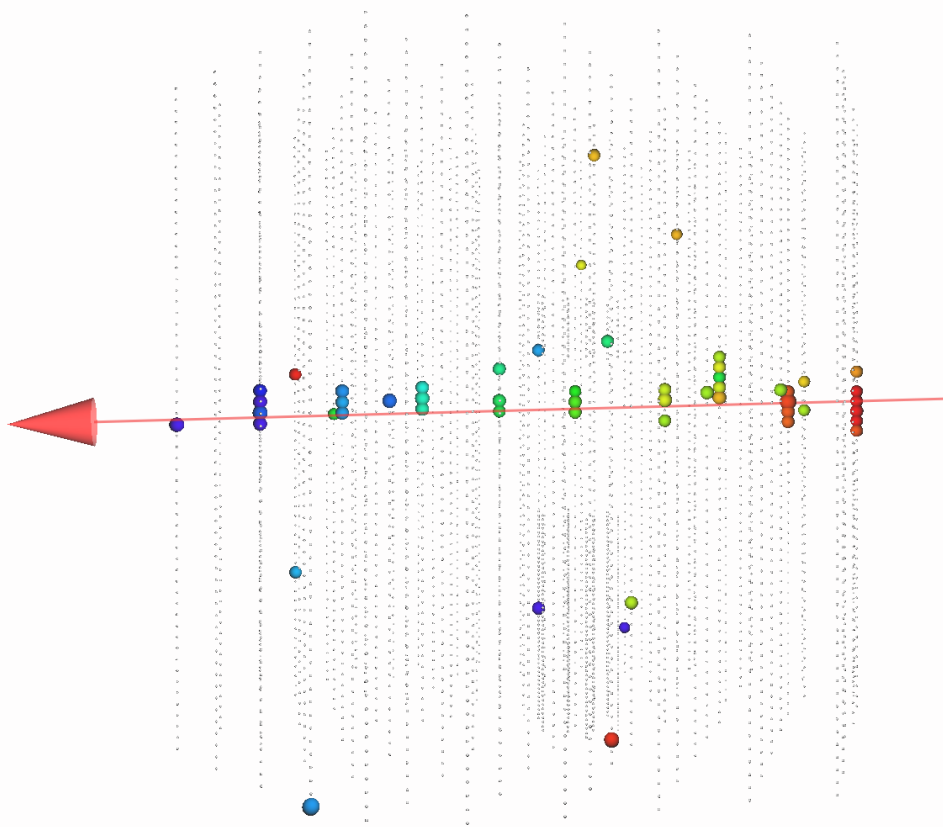


Figure 4.3: Depiction of a MC stau event in the IceCube detector. The stau was initialized with an energy of 23 TeV at a zenith angle of 88.7° and has been reconstructed to 573 GeV with a direction of 88.5° in zenith.

5 | PARTICLE AND DETECTOR SIMULATION

On their way through the detector muon and stau emit Cherenkov light. The amount of light emitted is proportional to the energy lost [95] and depends on their energy when entering the detector. The PMTs of the detector register the emitted Cherenkov photons and the information is grouped to events. Series of events then undergo different reconstruction algorithms and pass through several filter levels of an event selection process in order to get the most pure sample of the desired signal.

For the stau signal of our analysis, we exploit the suppression of stochastic losses by the stau mass (section 4.4) and search for an excess of low energy events. Regarding this definition, a region with an advantageous signal over background ratio is necessary in order to yield a significant result.

In Figure 5.1, we show the presumably most sensitive region for our signal according to theoretical predictions by [1]. Shown is the simulated signal and background data with respect to the incident zenith angle assuming two different stau masses. The background distributions in combination with the signal allow for a clear view on what angular bins the analysis is most sensitive to.

In the following chapter, we provide information on our simulation details regarding the complete process from stau production over stau event detection to sensitivity measurements. The first section covers the generation of staus happening at the primary interaction and inside air showers. Here, we also explain the subsequent propagation of the staus towards the detector. Combined, production and propagation then yield the stau flux at the surface of IceCube.

Thereafter, we provide details on the behavior of staus and muons inside the detector and explain the reconstruction algorithm and event selection used in our analysis. This includes a more fundamental handling of the propagation and light emission of the particles in ice and the detector's response to it.

After a description of our background sources, we explain the working principle of our used event selection. Here we go into detail about the different layers of the selection and the influence on stau signal and background. The final section is dedicated to the calculation of the signal acceptance in form of effective areas which represents a key part of our analysis. Furthermore, we explain how they are applied to yield the event rates of staus and provide two different measures for χ^2 -measures used in our analysis.

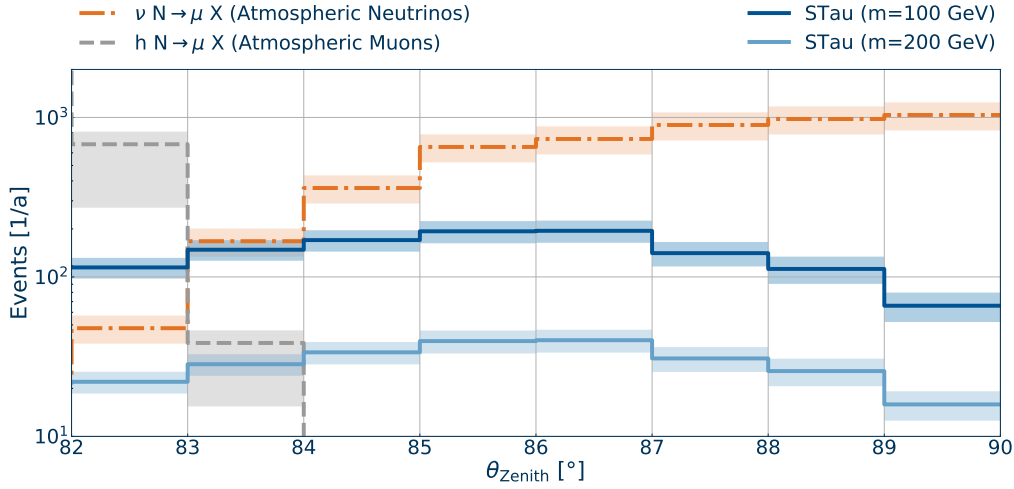


Figure 5.1: Predicted number of stau and muon events in IceCube per year as a function of the arrival direction in form of the zenith angle. The data was courteously provided by [1]. For the stau events a pure Drell-Yan production and masses of 100 and 200 GeV have been assumed, dark and light blue respectively. The muon events are shown separately and divided in their contribution from hadronic interactions (gray, dashed) and from neutrino interactions (orange, dash-dot). The shaded regions of each curve show the model uncertainties.

5.1 STAU FLUX AT DETECTOR SURFACE

To determine the rate of staus at the detector $[\frac{1}{m^2 s}]$, we simulate the stau generation in air showers and propagate them to the surface of IceCube. We start with a model for the primary cosmic ray flux and generalize the proton-proton cross section described in section 2.2. The combination of both provides us with the number of staus generated in the primary interaction.

Although we expect staus from primary interactions to account for the majority of the flux, we also simulate the production in secondary interactions. Therefore we model the evolution of the air shower with MCEq ([96]) and isolate the proton flux at different slant depths. At every level of penetration we apply the probability $P_{\tau}^h(E)$ from Equation 3.3 to the proton flux and obtain the number of staus produced.

This method is only applicable because of the low cross section for the stau production. Namely for it to be valid, the amount of energy lost due to the stau generation ought to be insignificant compared to other shower processes. For higher cross sections, the influence of a stau generation process on the evolving shower would no longer be negligible and require a different calculation.

So far, the simulations provide us with the energy dependent stau flux at different heights

in the atmosphere. For an energy dependent stau flux at the detector surface, it is necessary to propagate the stau over the remaining way. From every depth we thus calculate the energy lost on the remaining path according to Equation 2.3. In the end, we merge the stau fluxes that were propagated from every level of the atmosphere to obtain a continuous flux spectrum at detector level.

The simulations were done for different stau masses from 50 GeV up to 1000 GeV at zenith angles from 70° to 100° . A representation of the stau flux at the detector surface for a stau mass of 100 GeV and three different angles is shown in Figure 5.2. We observe that higher incident angles yield a lower stau flux at the detector. This is the result of the increasing amount of material staus need to overcome for an increasing zenith angle (Figure 5.4). At lower angles, staus do not lose as much energy on their way to the detector as it is the case for higher angles. Hence, more staus survive the journey and contribute to the flux at the detector. The sharp feature of the stau flux observed for any angle is related to a current software requirement of relativistic staus.

In the simulation process we use a combination of flux (Sibyll2.3c [97], EPOS-LHC [98], QGSJET-II [99] and DPMJET-III [100]) and interaction models (Gaisser-Hillas H3a, H4a [56] and Gaisser-Tilav Gen 3 and 4 [101]). From the results, we construct an average primary flux value, that is used in our analysis. In our case of a sensitivity study that neglects systematic uncertainties this treatment is sufficient, especially when looking at the errors of the energy reconstruction.

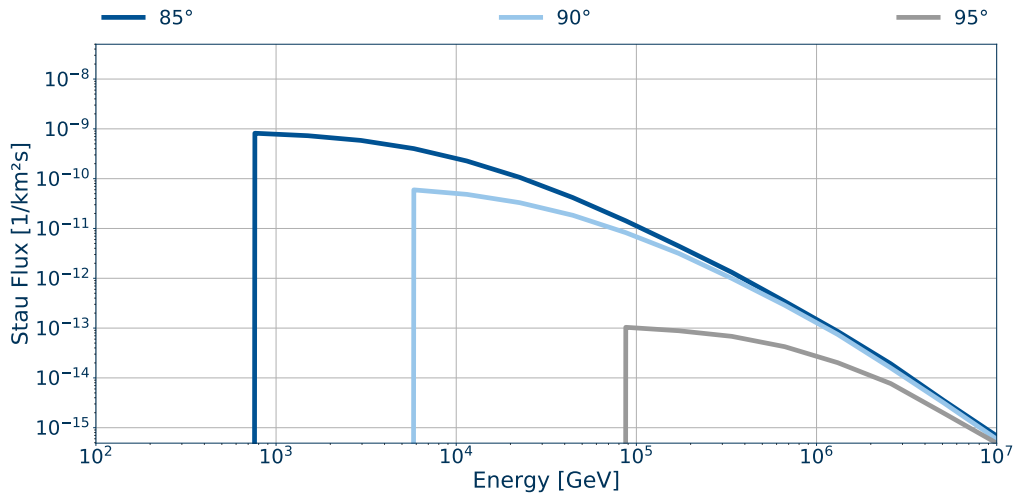


Figure 5.2: The flux of staus at the IceCube detector for three different directions in zenith angle assuming a mass of 100 GeV.

5.2 PARTICLES INSIDE THE DETECTOR

From theory we know that muons and staus produce track signatures inside the detector (see section 4.3). We also expect staus of any energy to imitate the track signal of low energy muons. In order to validate our theories, we evaluate how the detector responds to passing muons and staus.

We generate 500 000 events of evenly distributed random direction and energies between 100 GeV and 10 TeV that follow a E^{-1} power law. For the particle propagation through the detector and the corresponding energy loss simulations we use the PROPOSAL package [102]. Based on the energy loss pattern, photons are generated and propagated via the CLSim package [103].

During this process, assumptions about the depth dependent absorption and scattering lengths in the ice have to be made. The values used for the simulation in this work are found in the description of the ice model in [82]. After the Photon propagation, the response of the individual DOM modules is simulated. Charges and arrival times measured are noted and saved in the format of actual experimental data to be processed by event reconstructions and selections later on.

5.3 EVENT RECONSTRUCTION

The reconstruction of energy and direction takes up a crucial role in the analysis. Based on the time, location and amount of hits registered by the DOMs, software infers the decisive parameters of the event. This iterative process usually starts with a first guess pattern recognition, followed by advanced likelihood algorithms.

In the following we restrict ourselves to the reconstruction technique of track signatures for that both, signal and background, produce tracks inside the detector. More details on the event types observed in IceCube can be found in section 4.3.

The energy estimation of through-going muon tracks is complex and only provides lower limits because of the indefinite travel length before and after the detector. In contrast to that, the angular reconstruction profits from the extent of the track and its large amount of hit DOMs.

ANGULAR RECONSTRUCTION (SplineMPE) The estimation of directional information is based on a combination between likelihood algorithm, probability density function (PDF) and a first guess muon track parametrization. Caused by the interplay between different methods for all three components, we observe variations in the result. While some combinations are computationally extensive, they are also more accurate in their estimation. We restrict ourselves to the explanation of a small variety of individual methods for each component. Primarily, however, we focus on the combination used for our analysis.

Before applying specific likelihood functions, a first track hypothesis (H) is established. H models the track as a particle at the speed of light c . The path is further parameterized by a directional unit vector \mathbf{d} and a point of origin \mathbf{x}_0 at t_0 . This parametrization neglects the stochastic energy losses of the particle and serves as a first guess pattern for many likelihood reconstructions related to IceCube, including the one used in our analysis.

$$H : \mathbf{x}(t) = (t - t_0) \cdot c \cdot \mathbf{d} + \mathbf{x}_0. \quad (5.1)$$

In Figure 5.3 we show schematically the path of a charged particle from the track hypothesis, together with the Cherenkov light sent out towards the DOMs. We see illustrated, that the Cherenkov photons are scattered on their way through the ice and reach the DOMs later than they would in vacuum. The delay of a photon is thereby not only dependent on the travel length of the photon but also on the local optical parameters of the ice (see section 5.2).

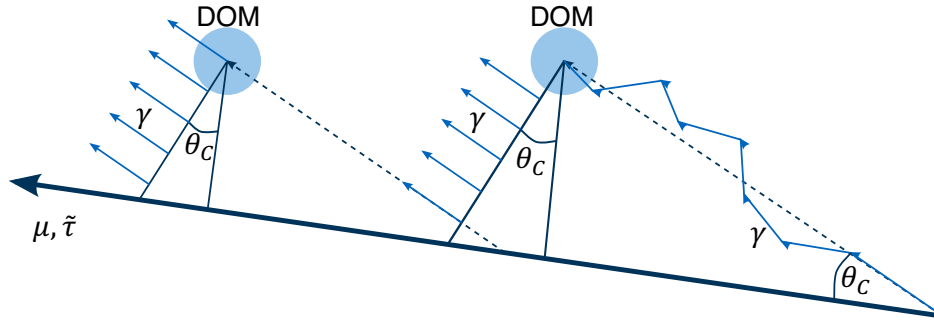


Figure 5.3: Depiction of the propagation of Cherenkov photons emerging from a charged particle traveling through a medium. As an example we show two DOM modules that capture the Cherenkov light at different times, depending among other things on the geometry of the track and the optical ice properties.

In order to improve the resolution of the first guess track hypothesis, we consider the displayed scattering effect in Figure 5.3. Because of the random nature of light propagation, an exact analytical solution is no longer feasible and the most probable track is established with maximum likelihood approaches. This results in the optimization of the five free parameters defining the track in H ($\mathbf{x}_0 = (x, y, z)$, $\mathbf{d} = (\theta, \phi)$).

For convenience, we define the time residual t_{res} , that represents the difference between the observed arrival time $t_{observed}$ and the geometrically possible arrival time t_{geo} .

$$t_{res} = t_{observed} - t_{geo}. \quad (5.2)$$

The PDF can then be expressed as a function of the time residual ($p(t_{res}^j | \mathbf{x}_k, H)$). We

then construct a first likelihood of every detected pulse j at every DOM k with position \mathbf{x}_k : [104]

$$\mathcal{L}_{SPEAll} = \prod_i^{N_{DOMs}} \prod_j^{N_{Pulses,i}} p(t_{res}^j | \mathbf{x}_k, H). \quad (5.3)$$

The likelihood function is indexed *SPEAll*, as it is constructed as a Single-Photo-Electron (SPE) likelihood using all PMT pulses of each DOM. However, it has been established that the usage of all pulses from a DOM, makes the likelihood function sensitive to unwanted PMT effects. In this regard, it is beneficial to use only the first of all pulses from the respective DOM. The photon that triggers the first pulse of a PMT usually exhibits the least amount of scattering processes and is thus more robust against systematical errors from optical properties [104].

In the end, the PDF is then modified and used to form the Multi-Photo-Electron likelihood (MPE) [95]:

$$\mathcal{L}_{MPE} = \prod_i^{N_{DOMs}} p(t_{res}^{1,i} | \mathbf{x}_k, H) \cdot N_{Pulses,i} \cdot \left(\int_{t_{res}^1}^{\infty} p(t | \mathbf{x}_k, H) dt \right)^{N_{Pulses,i}-1}. \quad (5.4)$$

As a next step, the MPE likelihood is interfaced with a parametrization of the PDF function p for the photon arrival times. This can be done analytically with the Pandel function from [105] (see also [95]) or with smooth spline functions interpolating between location dependent simulations of the arrival times [106].

Altogether, it turns out, that the usage of the analytical Pandel function is computationally less extensive than using spline-based PDFs. However, interfacing spline-based PDFs yields the best angular resolution in combination with the MPE likelihood. This approach is called `SplineMPE` and will be our angular estimator throughout the analysis.

ENERGY RECONSTRUCTION (`SplineMPE_TruncatedEnergy`) The nature of the energy losses of staus and muons and how they compare are described in section 2.2. Throughgoing tracks of any particle type deposit only part their energy inside the detector. The unknown point of origin and the remainder of energy when leaving the detector make a calorimetric approach unsuitable. Another consequence, makes any estimator of energy only a lower bound on the particles energy at their generation vertex.

The particles energy can only be inferred from the fraction of the path that leads through the detector. An energy estimation for track signatures therefore relies on the differential energy loss dE/dx described by Equation 2.3. In [107] both, a conventional approach for the energy estimation with dE/dx and an alternative using the truncated mean of dE/dx is explained.

In either approach, the photoelectron yield is expected to be directly proportional to the energy loss of the particle. For the conventional approach, one builds the sum over all photoelectrons registered by all DOMs along the track ($N_{observed}$). Now, assuming a track with a fixed energy loss of 1 GeV/m, one calculates the overall expected number of photoelectrons registered for this case ($N_{expected}$). In the end, the dE/dx value of the track is equal to

$$dE/dx = \frac{N_{observed}}{N_{expected}} \cdot 1 \text{ GeV/m}. \quad (5.5)$$

This linear relationship works well as an approximation for energies above ~ 1 TeV [107]. The obtained values however, still show a large spread that is explained by the stochastic losses. As of the non-linear nature of the stochastic losses, many events will be reconstructed to a higher energy. In order to remove the bias a truncated mean energy estimator is introduced.

For the truncated mean energy estimator, every event track is segmented by planes perpendicular to the direction, binning every sensor accordingly by their location [107]. Similar to the conventional approach, dE/dx is determined by the ratio of the observed over the expected amount of photoelectrons (see Equation 5.5). However, the ratio is now calculated for each bin separately. The fraction of bins with the highest ratios are selected and discarded in an optimized manner discussed in [107]. In the end, the truncated dE/dx energy estimator uses again the sum of all observed and expected photoelectrons over what bins are left of the track and determines the energy of the particle with the resulting truncated mean of dE/dx .

If the truncated mean estimator uses `SplineMPE` for the segmentation of the track, we end up with what is called `SplineMPE_TruncatedEnergy`. This energy estimator is used throughout the analysis and will be shown as reconstructed energies in this work unless otherwise stated.

5.4 BACKGROUND

The most dominant sources of background are muons produced in hadronic interactions in the atmosphere (atmospheric muons) and those produced in neutrino interactions (atmospheric neutrinos). Background distributions vary depending on energy and incident angle. This alteration is often related to the material and the distance the particles have to pass through before they reach the detector.

For a simplified IceCube scenario, different materials and their distances have been plotted in Figure 5.4. We distinguish between three overall types of materials that particles traverse on their way to the detector. The different sources of background are thereby affected differently by each material.

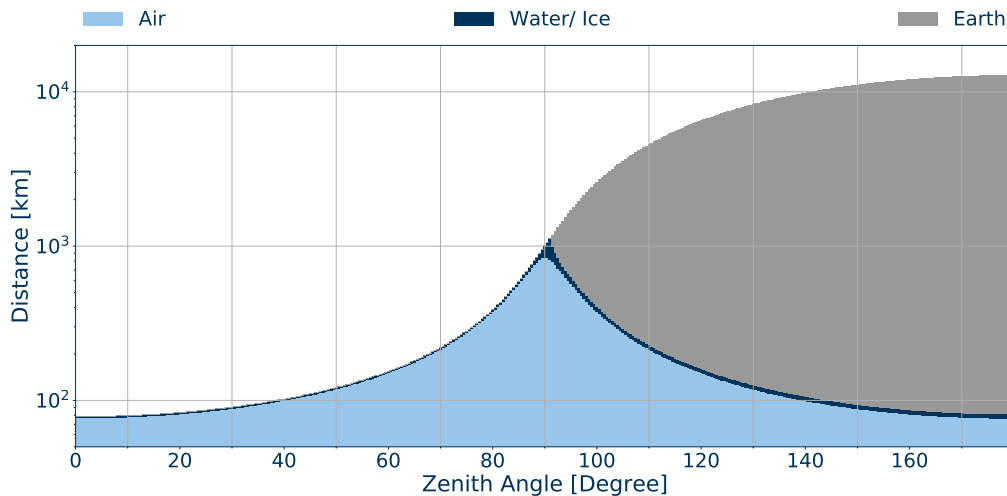


Figure 5.4: Approximation of the different materials passed in the way to the detector in relation to the zenith angle. The representation is based on the assumption of 80 km of atmosphere surrounding the earth covered with a 3.5 km layer of ice/ water.

Staus are expected to behave like low energy muons (section 4.4) making a separation between the two signals difficult. An indication for staus is thus an excess of low energy muons registered by the detector. For this reason, a precise knowledge and modeling of our background is very important. In addition, the low stau flux resulting from the low cross section (Figure 2.3) necessitates a low background to make an excess significant. We thus consider the following two main sources for muons at IceCube and assess their contribution to the background of our analysis.

ATMOSPHERIC MUONS Muons from atmospheric showers make up a direct source of background for our analysis. Especially in the low energy region, where staus and muons behave the same, they represent the majority of background events. The amount of muons produced in an atmospheric shower exceeds the one required for a possible detection of an excess by far. After their generation however, muons undergo permanent energy losses and are eventually stopped before they even reach the detector.

A 10^5 GeV muon loses 30% of its initial energy by traveling one kilometer in ice (Figure 4.2). When looking at the distance the particles have to travel before they reach the detector (Figure 5.4), we see that for an increasing zenith angle more and more energy is lost on the way. Thus, the background from atmospheric muons decreases steadily when approaching the horizon (zenith = 90°). At some point, the passage through the composition of materials stops every muon produced in an atmospheric shower outside of the detector. Even high energy muons will not be able to reach the detector anymore and the detector is shielded against atmospheric muons.

The atmospheric muon estimate (gray, dashed) of [Figure 5.1](#) rests upon this theory and predicts no significant rate of muons from hadronic interactions above 84° . This is supported by an investigation of the atmospheric muon flux measured by IceCube in [108]. Reconstructed zenith angle and reconstructed energy indicate a cut-off at $\sim 84^\circ$, which is in good agreement with the predictions. Above this angle, the amount of atmospheric muons registered by the detector becomes negligible and other sources of background become relevant.

MUONS FROM NEUTRINOS Regardless of their origin, muon neutrinos pose a noticeable source of background. Our analysis hereby concentrates primarily on atmospheric and astrophysical muon neutrinos. Although neutrinos of other flavors are capable of producing muon track signatures similar to staus, their contribution to the background is negligible and is thus disregarded completely.

As our stau signature compares to a low energy muon, any interaction of a muon neutrino potentially accounts for our background. Only muons that arise from an interaction within the detector ('starting tracks') can be discriminated against stau tracks. Reason for this, is that in our analysis staus are only produced in air showers and will thus never leave a starting track inside the detector.

However, the muon background at the detector resulting from the astrophysical and atmospheric neutrino fluxes consists of an interplay between many properties. Not only do the neutrino fluxes itself vary for different zenith angles and energies. Conditional upon the geometry and with it the surrounding mass of target material, the fluxes of astrophysical and atmospheric neutrinos translate differently into the muon flux that accounts for the background at the detector.

While muons lose energy continuously, neutrinos travel long distances without interacting because of their low interaction cross section. If the neutrino flux however is high like the atmospheric flux, enough muons are produced to hide the stau signal. How many neutrinos ultimately commute into muons however, depends on the distance traveled in the different materials. From their generation vertex, the muons lose energy and have to propagate the remaining way in order to account for the background. In [Figure 5.1](#) the muon background from neutrino interactions is displayed in orange (dash-dot)

More details on the handling of background are found in the section about the [Event Selection](#). There we reflect on the influence of the selection on the different sources of background events.

5.5 EVENT SELECTION

The construction of an event selection in IceCube involves a long, enduring process. Bearing in mind the scope of this thesis, we thus decide to use an existing selection that incorporates a large overlap with the specifications of our stau search. The chosen event selection, is optimized for neutrino induced through-going tracks of muons, whose investigation necessitates a significant reduction of the main background from atmospheric muons ($\gtrsim 2$ kHz) [109].

Both event signature and background source partially match the requirements of an event selection for our analysis. Staus appear in form of minimally ionizing, through-going, muon like tracks (see section 4.4) and part of our background is represented by atmospheric muons (Figure 5.1). However, another background source of our analysis consists of neutrino induced muon tracks. Hence, for the purpose of a first sensitivity study this event selection is sufficient but remains unoptimized.

Many of the MC events generated in our simulation, produce insufficient DOM hits in order to be processed by the reconstruction algorithms. A first event selection is thus performed by a trigger, choosing only events with enough photons registered by the PMTs of the detector. In the event selection used for our analysis, two additional levels (*Level2*, *Level3*) are introduced after the trigger to clean out unwanted background events (for details see [110, 111]). Further improvements on the selection are made with the aid of supervised machine learning techniques, explained in [104, 109] and introduce the event selection's *Final Level*.

The various filter levels of the event selection aim for a pure sample of muons induced by atmospheric neutrinos. After the trigger level, *Level2* and *Level3* the remaining events are too plentiful to perform accurate reconstruction algorithms with reasonable resources. Cuts are thus applied on quantities that supply sufficient information and take small computational effort.

In the *Level2* filter, events with extremely high energy ν with a poor fit result from the *SPEFirst* algorithm interfaced with the *Pandel PDF* (section 5.3) are thrown out [104]. *Level3* cuts target more specific parameters with information about the event topology. These include for example, the number of DOM hits in a given time window or the distance between first and last DOM with directly projected photons on the reconstructed track [104].

In combination with a general cut selecting only zenith angles θ above 85° , the event rate is reduced to ≈ 1.5 Hz [109]. The aim of the angular cut is to select a region with a theoretically low background of atmospheric muons. As the distance towards the detector and through the ice increases with increasing θ more and more atmospheric muons fail to reach the detector. Investigations of [108] support a cut off at $\theta 85^\circ$ to be reasonable.

At this point, the rate dropped low enough that more accurate reconstruction methods become feasible. However, mis-reconstructed atmospheric muons still make up the majority

of the signal region [109]. To further clean the sample and reach the *Final Level* of the event selection, two boosted decision trees (BDTs) are trained that distinguish between signal and mis-reconstructed background events [104, 109].

Each of them takes on a different role in the cleaning process. One of the trees cleans the remaining events from mis-reconstructed cascade event topologies (section 4.3). The other one filters out tracks caused by atmospheric muons. In combination this achieves a sample purity of 99.87% [109].

In order to set the event selection in context with our sensitivity study, we look at Figure 5.1. There we see, that our most sensitive region concerning the arrival direction is between 82° and 85° in zenith angle. Through the cut-off of events below 85° in the event selection, this region becomes thus inaccessible for our analysis. How big of an effect this has on our results is discussed in chapter 8.

5.6 CALCULATIONS

All subsequent processing in this work involves only the events that remain on the *Final Level* of the event selection, unless otherwise stated. Those events passed every introduced cut described in the previous section 5.5 and serve as our best sample. With this sample of events we illustrate the resolution of the angular and energy reconstruction method used in our analysis for staus and muons. In addition, we use the event sample to calculate the signal acceptance in form of effective areas. Convolved with the simulated stau flux at the detector, the effective areas then provide us with the rates for our stau signal.

EFFECTIVE AREAS Effective areas are a representation of how well a certain particle type is detected and how much of an area is thus covered by the detector. They are calculated with the remainder of the events after the event selection N_{final} (*Final Level*), the MC events in total N_{total} and the etendue E of the detector. E characterizes the spread of light able to reach a given object in area and solid angle. In our case, the object is the IceCube detector, which we approximate by a cylinder with height 1400 m and a radius of 700 m for the calculation of E in our analysis. The equation for the effective area A is then written as

$$A = \frac{E \cdot N_{final}}{4\pi \cdot N_{total}}. \quad (5.6)$$

This formula yields an overall effective area for the respective particle type. However, effective areas change for different zenith angles and energies. The cuts of our event selection influence N_{final} directly. Depending on zenith and energy, varying amounts of events survive the cuts and lead to a difference in effective area. In addition, the

etendue E depends on the selection of the zenith angle θ . So for an angle selection $\theta_s = \theta_{min} - \theta_{max}$ our formula for the effective area looks like this:

$$A = \frac{E(\theta_s) \cdot N_{final}(\theta_s)}{2\pi \cdot (\cos(\theta_{min}) - \cos(\theta_{max})) \cdot N_{total}}. \quad (5.7)$$

An additional selection of an energy range, yields the effective areas for different energy/zenith bins that are used throughout our analysis. With our definition, it is possible to calculate the effective areas at every level of our events selection, simply by exchanging N_{final} by the amount of events at the desired level.

CHI²-MEASURES The multiplication of the effective areas in the energy/zenith bins and the simulated stau flux at the detector surface from section 5.1 yield the stau signal rates (R_{Signal}). Together with the rates of the background ($R_{Background}$), we can calculate a first naive χ^2 value for each individual bin on the energy/zenith grid.

$$\chi^2 = \frac{R_{Signal}^2}{R_{Background}}. \quad (5.8)$$

The resulting χ^2 -map is used to illustrate the most sensitive region and gives a rough estimate on the power of the analysis. Our analysis however, aims for a more elaborate sensitivity on the stau mass. We are thus looking for a significant excess to accept the hypothesis of the existence of the stau. With increasing mass, we see a decrease in cross section, meaning fewer stau events for higher masses. A significant excess with 90% confidence level is therefore directly linked to the assumed mass of the stau. Over this connection, we determine the mass limit up to which we can exclude the existence of a stau, as we otherwise would have observed an excess in events.

For the calculations of our mass limit sensitivity, we bin our signal and background rates in energy and zenith angle (R_{Signal} , $R_{Background}$) and create a 2D grid for both signal and background. We generate 1×10^5 outcomes ($R_{Poisson}$) for each bin of the grid with an underlying Poisson distribution where λ is equal to the signal and background rate. With 1×10^5 Poisson outcomes for signal and background in every bin, we calculate a χ^2 for each individual bin according to

$$\chi^2 = \frac{(R_{Poisson} - R_{Background})^2}{R_{Background}}. \quad (5.9)$$

Afterwards we sum the bins of the grid for each of the 1×10^5 different outcomes for signal and background and obtain an overall χ^2 value for every outcome. With 1×10^5 χ^2 values for both signal and background, we create two different χ^2 distributions. We now require that the median of the χ^2 background distribution equals the 10th percentile of the χ^2 signal distribution. For each mass, we then find the multiplication factor that satisfies

the equation when applied to the signal rates. The mass at which the multiplication factor is equal to one represents the current sensitivity of our analysis.

6 | FINDINGS

In this chapter we present the findings of our analysis and the included MC simulation. We start off with the resolution of our event reconstruction methods for energy and angle (section 5.3). Afterwards we show the effective areas of muons and staus and illustrate the influence of the event selection (section 5.5). In addition, we show the effective area of staus in three zenith bins ($85^{\circ}\pm 0.5^{\circ}$, $90^{\circ}\pm 0.5^{\circ}$, $95^{\circ}\pm 0.5^{\circ}$) that concur with the angles in our illustration of the stau flux from Figure 5.2.

Together with the stau flux at the detector surface, effective areas yield the rates of our stau signal. The rates are displayed individually and in comparison with the background source of muon tracks induced from atmospheric neutrinos.

With the combination of signal and background we calculate and display χ^2 measures on a 2D grid of zenith angle and energy bins. From the χ^2 maps of different stau masses we are able to extract a sensitivity and illustrate the state of our analysis.

6.1 EVENT RECONSTRUCTION

In section 5.3 we describe the working principle of our reconstruction methods for angle and energy. Figure 6.1 shows the resolution in zenith angle for stau and muon events with the `SplineMPE` reconstruction. For each particle type, the respective bars illustrate the 68% region around the median (orange) in the respective energy bin. In the displayed energy range, the angular resolution of the muon (light blue) improves steadily with increasing energy. For the staus (dark blue), no event of the first energy bin survives the event selection, hence no bar is displayed. After some fluctuations, we observe a convergence to stable median angular difference of around 1° .

Both observations are well explained by the nature of the energy deposition for the different particles. Higher energy muons deposit more energy inside the detector, triggering more DOMs and thus producing more detailed information to perform calculations upon (Figure 4.2). The more information is given to the reconstruction algorithm the better its performance. Hence for the muon, we see an improving angular resolution at higher energies because it deposits more and more energy on its way through the detector.

From Figure 4.2, we know that the stau's energy deposit inside the detector shows no

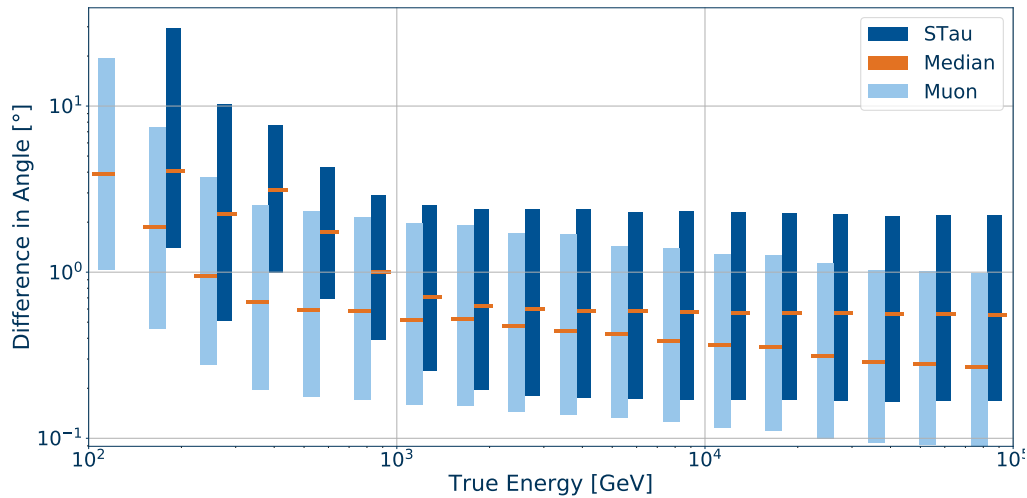


Figure 6.1: Resolution in zenith angle for stau and muon events using the `SplineMPE` reconstruction (section 5.3). The bars represent the 68% region around the median (orange). No stau events are reconstructed in the first energy bin, hence no bar can be displayed.^{1,2}

significant change after it is able to traverse the detector completely (~ 280 GeV). This peculiarity makes the angular resolution approach a stable median value for energies above ~ 1100 GeV. The gap between the point where we would expect no more information to be added and thus the resolution to be stable, at 280 GeV, and 1100 GeV is caused by essentially one thing.

For once, one has to keep in mind that not all of the theoretically deposited energy is registered by the DOMs. An interplay between absorption, scattering and the PMT efficiency causes a lower photon count. Thus, less information is gathered by the detector than is theoretically provided by the deposited energy. In combination with the efficiency of the reconstruction algorithm, this leads to an increased point of convergence for the staus angular resolution.

The energy resolution of stau and muon events using the `SplineMPE_TruncatedEnergy` estimator described in section 5.3 is depicted in Figure 6.2. At the top, we see the energy reconstruction for staus and its independence on the true energy, where in the bottom plot we see the result of an intact energy estimation of muons with a small bias at low energies.

Both subplots agree with theoretical predictions and confirm previous considerations. While we see the desired linear correlation between true and reconstructed energy for muons, the staus are reconstructed to an energy band between 100 GeV and ~ 2000 GeV, independent on their injected true energy. This behavior illustrates the difference in energy loss and thus the energy deposition (Figure 2.4, Figure 4.2).

The suppression of stochastic energy losses causes staus to deposit only a fraction of their actual energy inside the detector. Compared to the muon, the energy loss of the stau seems constant for the energy range we are interested in ($100 \text{ GeV} - 1 \times 10^5 \text{ GeV}$). Hence, the reconstruction algorithm estimates the stau energies as if it were low energy muons. The fact of that reassures us on our excess event search in the low energy region.

For increasing stau energies, the deposited energy theoretically increases with a fraction of $\sim 1/m_{\tilde{\tau}}$ from the stochastic energy losses (Figure 4.2). With our energy resolution, we

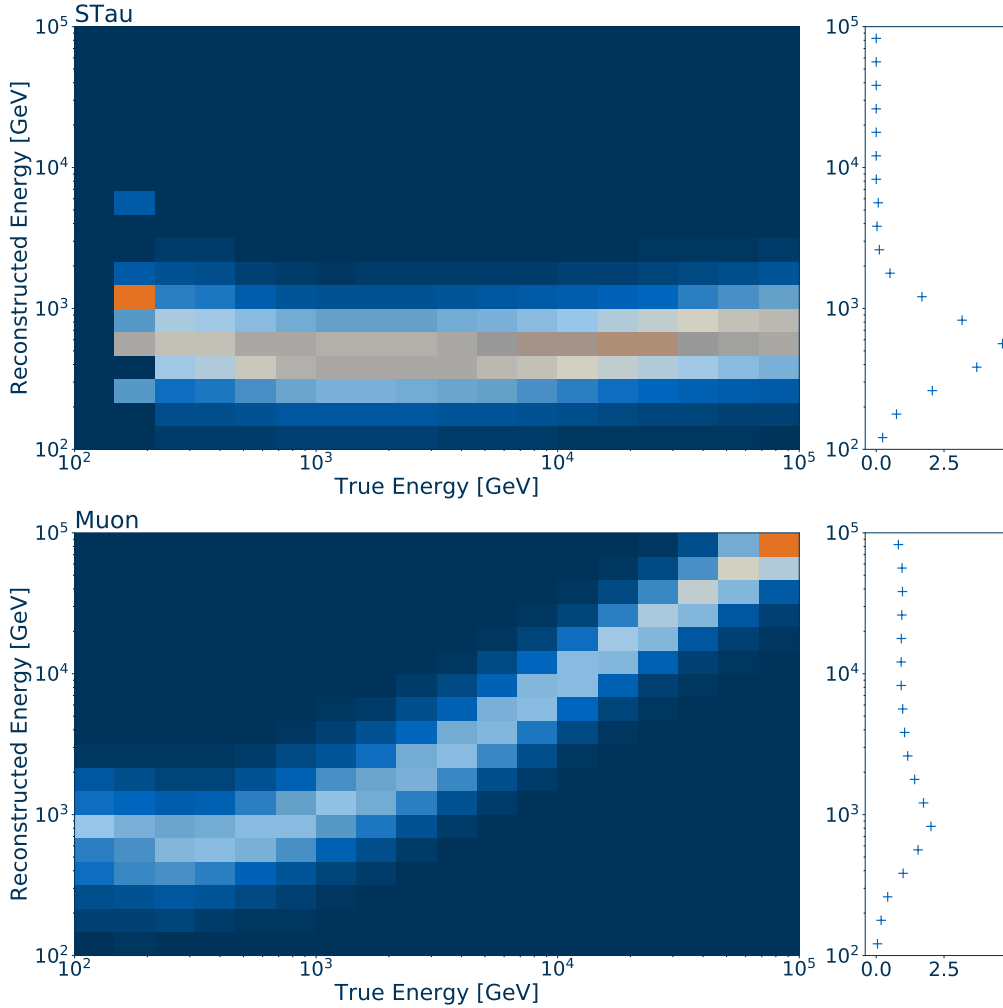


Figure 6.2: Resolution in energy for stau (top) and muon (bottom) events using the `SplineMPE_TruncatedEnergy` reconstruction (section 5.3). The plots show a 2D histogram with the reconstructed energy on the y-axis with respect to the true MC energy on the x axis. Each column of true energy is normed with its sum of events. On the right side, we show the marginal distributions of the events, being the sum over every row.^{1,2}

are able to observe this increase for energies above 10^4 GeV. There we notice a shift of the reconstructed energy distribution to higher reconstructed values.

Overall, the reconstruction methods prove well for our analysis and enable us to proceed on our excess event search in a zenith region between 80° and 95° and reconstructed energies between 100 GeV and 1000 GeV. However, we notice a bias with the reconstruction of low energy muons that accumulate in our region of interest. Regarding our sensitivity, this accumulation will lower the signal to background ratio for later χ^2 calculations.

6.2 EFFECTIVE AREA

In section 5.6 we describe the meaning and calculation of effective areas shown in the following plots. Figure 6.3 and Figure 6.4 illustrate the influence of the different layers from our event selection (section 5.5) on the effective areas of muons and staus.

Data, labeled *Generation Level*, uses all generated MC events, whereas other displayed levels already include cuts and use only processed events. For every stage of our event selection we tighten our cuts on the events and thus alleviate our effective areas as seen in Figure 6.3 and Figure 6.4. For the muon effective areas in Figure 6.3, we include data from previous studies concerning muon effective areas in orange colors. These data indicate *Level2* and *Final Level* events from the used event selection and show good agreement with the data from our own muon sample. We see this as a validation of our simulation chain and assume that the calculations of our stau effective areas are correct as well.

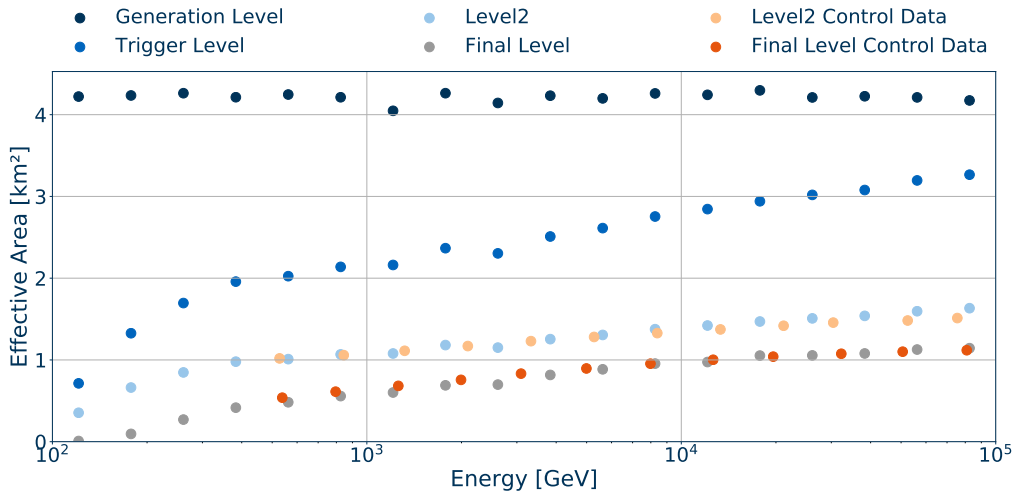


Figure 6.3: Effective area of muon events at different levels of the event selection.^{3,4}

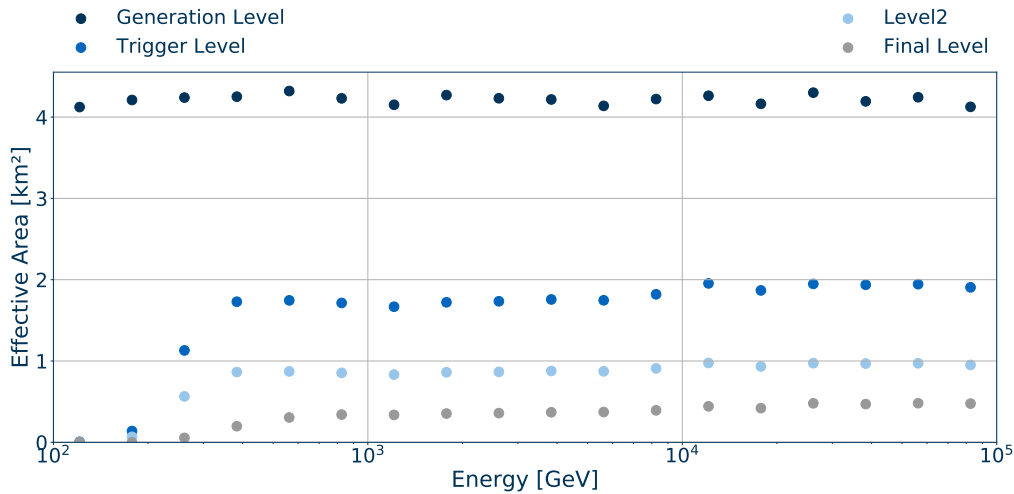


Figure 6.4: Effective area of stau events at different levels of the event selection.^{3,4}

In both plots, we note a fundamental difference that concurs with our previous findings (section 6.1). Similar to the muon resolutions of angle and energy, Figure 6.3 shows improving muon effective areas with increasing muon energy at all filter levels. The effective areas for staus on the other hand, build a plateau and stay constant independent of their energy (Figure 6.4).

This behavior is another reflection of the difference in the energy loss and deposition of muon and stau, seen in Figure 2.4 and Figure 4.2. As soon as the stau has enough energy to traverse the detector completely, the energy deposition does not increase any further. For muons, more energy is deposited and thus more events are recognized to account for the effective area. Stau events on the other hand, look the same independent of their energy, resulting in a constant effective area.

From the direct comparison between stau and muon effective areas in Figure 6.5, we infer that even before stochastic losses dominate the muon energy loss, stau effective areas are smaller. This discrepancy is due to our event selection that is not optimized for the minimally ionizing stau signature and instead searches for muon tracks. Note, that here again, we are able to resolve the small increase of the suppressed stochastic energy losses of staus as a slight increase in effective area towards higher energies.

Next to the display of muon and stau effective areas at different filter levels, we look at the stau effective areas binned specifically in three different zenith angle (Figure 6.6). We have chosen three angle bins in intervals of 5° beginning at 85° zenith, which is the lower cut-off of our event selection. From the comparison between the 90° and 95° data points, we argue that higher angles somewhat yield a higher effective area, at least in our angular range. However, the large difference to the effective area at 85° ($\mathcal{O}(2)$ magnitudes) is caused by another effect, namely the cut-off of the event selection.

The chosen zenith bins for the representation of the effective area align with the selected bins from the stau flux in Figure 5.2. We see there, that the stau flux attenuates with higher zenith angle while it is the opposite for the effective area. The convolution of both, effective area and flux gives us the stau rates. In this regard, it is particularly interesting to see, whether the higher flux for smaller angles compensates their lower effective area.

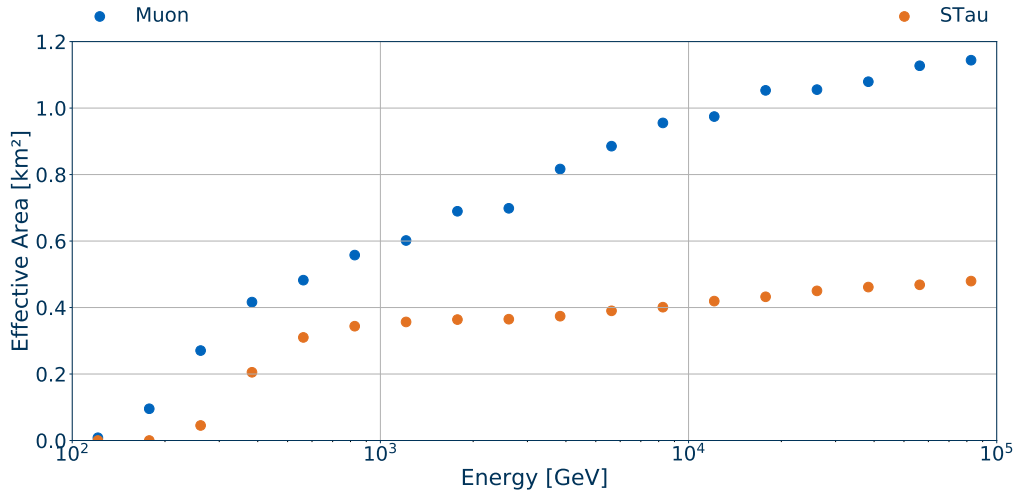


Figure 6.5: Effective area of stau and muon events.^{1,2,4}

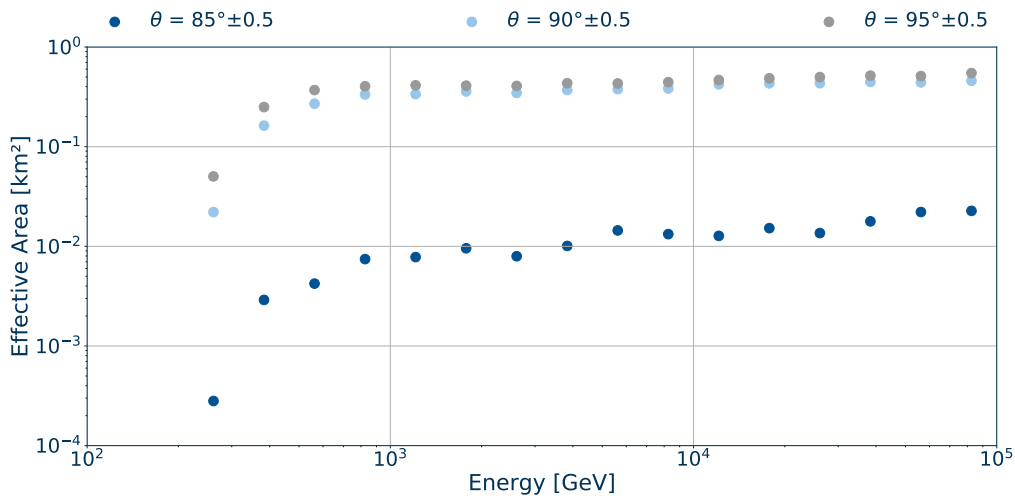


Figure 6.6: Effective area of stau events at *Final Level* for three specific zenith bins (85° , 90° and 95°).^{1,4}

6.3 STAU RATES

In the following we show the stau rates composed of effective area and stau flux in various different representations. We show a 3D representation of the stau rates in our region of interest to obtain a better view on the topology, as well as configurations of the integrated rates over angle and energy. The integrated rates are shown to reveal features of the energy reconstruction and our event selection.

Figure 6.7 shows the stand-alone stau rates for an assumed stau mass of 100 GeV on a energy/ zenith bin grid in 3D. On the side planes we show the marginal distributions as a sum over the respective dimension.

As a result of the event selection, we see our stau signal only in zenith bins above 85° in zenith angle. We additionally notice the desired accumulation in the lower energy regime, which is due to the constant energy deposition. From the marginal distributions, we infer that if the staus were to have a mass of 100 GeV, IceCube should see an excess of around six events per year in an energy range between ~ 450 GeV - 700 GeV. On the other side, when summing over the energies, IceCube should see an excess of five events per year in a zenith angle range between 87° and 88° .

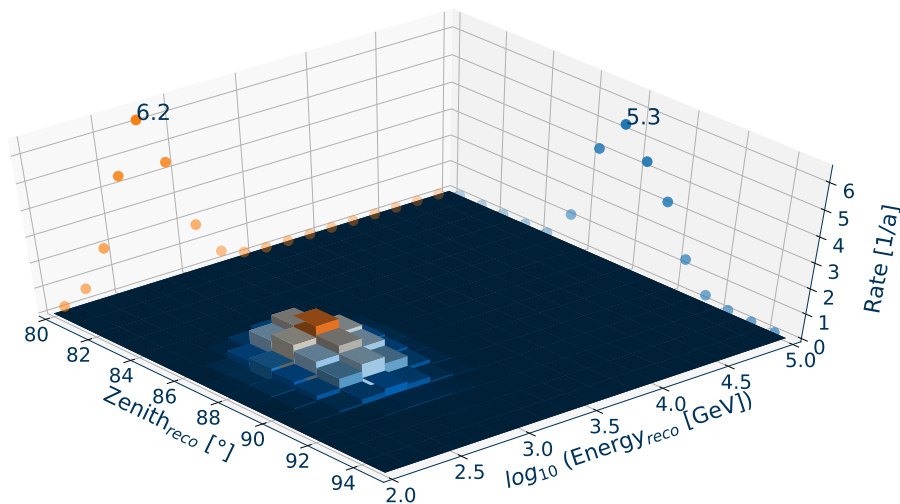


Figure 6.7: 3D representation of the stau rates on a energy/ zenith binned grid with integrated rates over energy and angle on the respective x-z and y-z plane.¹

In Figure 6.8 we portray the integrated rates over angles from 80° to 95° with respect to the reconstructed energy. We compare the rates for stau signals assuming a 50 GeV and a 100 GeV stau mass with the muon background induced by atmospheric neutrinos. This gives us a better overview on the rates in our region of interest and reveals the desired features of our energy reconstruction.

Comparing the stau rates of the different masses, we notice a strong reciprocal depend-

ence as expected from Figure 2.3. The stau rates differ by one order of magnitude for a doubling of the mass difference. Our bin with the highest amount of events is shown here more clearly compared to the previous plot and spans a range between ~ 450 GeV - 700 GeV.

As expected, the distribution of our signal appears similar to the distribution of events in the marginal plot of the energy resolution (Figure 6.2). In fact, also the bins with the highest event count are concordant. This affirms the coherence of our analysis.

As for the distribution of the stau signal, we see the peak of the background in the same bin as the accumulation in the energy resolution plot of the muon (Figure 6.2). Thus, the peak of the background distribution is partly caused by the reconstruction bias at lower muon energies. The difference between signal and background in this configuration amounts to a little more than one order of magnitude for assuming a stau mass of 50 GeV and more than two orders of magnitude for a stau mass of 100 GeV.

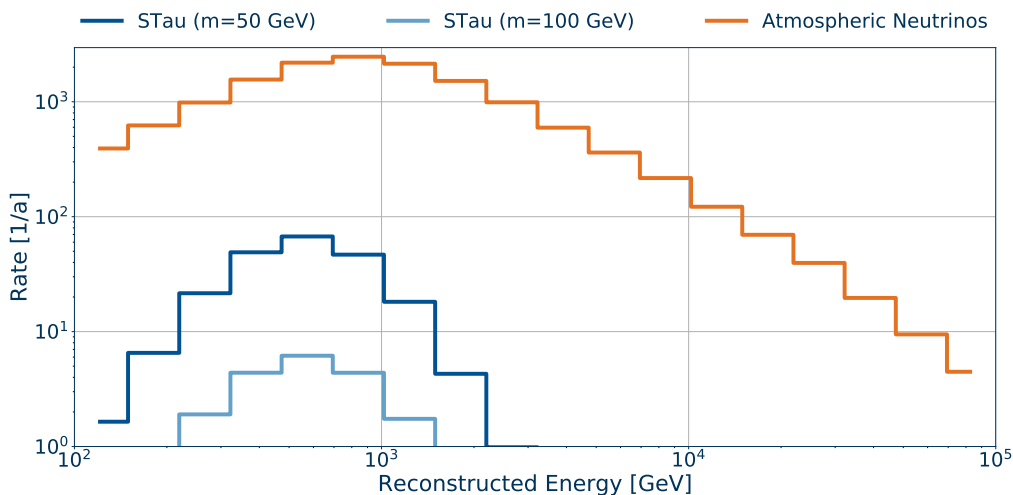


Figure 6.8: Event rates of staus for masses of 50 GeV and 100 GeV and the atmospheric neutrino background integrated over angles from 80° to 95° zenith.^{1,8}

Viewing the rates in an angular configuration in Figure 6.9, we notice the most apparent feature of our event selection. Signal and background, both incorporate a sharp cut-off for events below 85° . The trend of smaller rates for higher stau masses is observed here as well and yields approximately the same difference in rate for the same increase in mass (\sim one order of magnitude). However, we see that the difference between signal and background has shrunk in this configuration. In our most sensitive bins, the difference is now even less than one order of magnitude, for the 50 GeV stau signal.

For the display in Figure 6.9, we select only events with reconstructed energies between 100 GeV and 1000 GeV. We choose this selection as from our energy reconstruction we know that most of our events are reconstructed into that region. Figure 6.8 backs this fact and shows that only part of our signal is cut out, whereas our background is affected

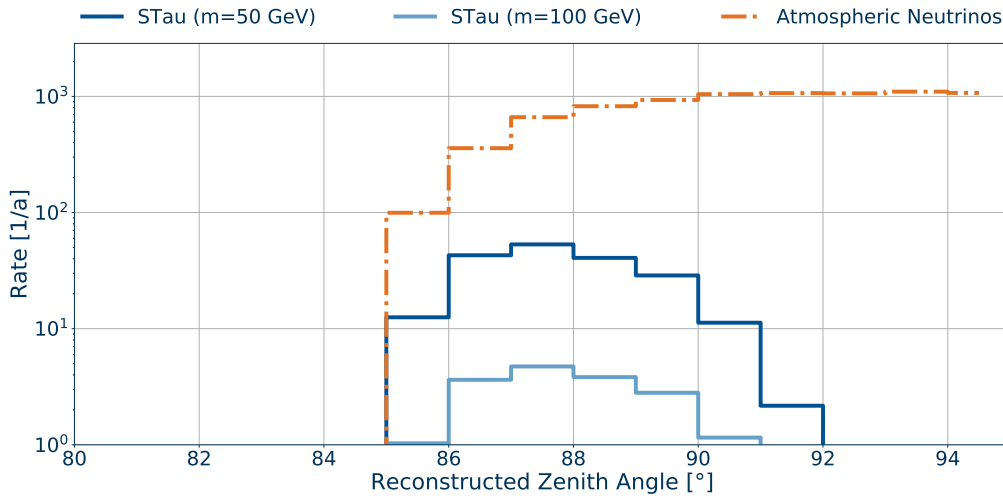


Figure 6.9: Event rates of staus for masses of 50 GeV and 100 GeV and the atmospheric neutrino background.^{1,5,8}

most by this cut. To get a better view on the sensitive bins, we introduced a χ^2 measure in section 5.6 that is used and shown in the next section.

6.4 STAU MASS LIMIT

One indicator for the most sensitive bins is the χ^2 measure constructed with Equation 5.8. In Figure 6.10 and Figure 6.11 we use the rates of stau signal and muon background for each bin and calculate the respective χ^2 on the energy/zenith bin grid. Note, that our two representations of χ^2 -maps are made with the rates for two different masses and varying years of observational data.

In Figure 6.10 we compare the rates of 100 GeV staus to the muon background over one year of data. The most significant bin in this configuration lies between 86° and 87° in zenith angle and between ~ 450 GeV - 700 GeV in energy. From the display we observe a circular attenuation of the χ^2 values around the maximum. Additionally, we recognize the cut-off from our event selection.

The sum over the χ^2 values gives a preliminary estimate on the power of our analysis. In order for the analysis to become significant at 90% confidence level, we require the sum over all χ^2 values of the map to be $\gtrsim 2.71$. From the values in Figure 6.10, we draw that we do not reach the said threshold with our combination of stau mass and duration. Thus, we have to increase the rates of our signal by for example assuming lower stau masses with the data of a longer time period. An example of the resulting effect is displayed in Figure 6.11.

There we assume a stau mass of 50 GeV and an observation over ten years, concordant

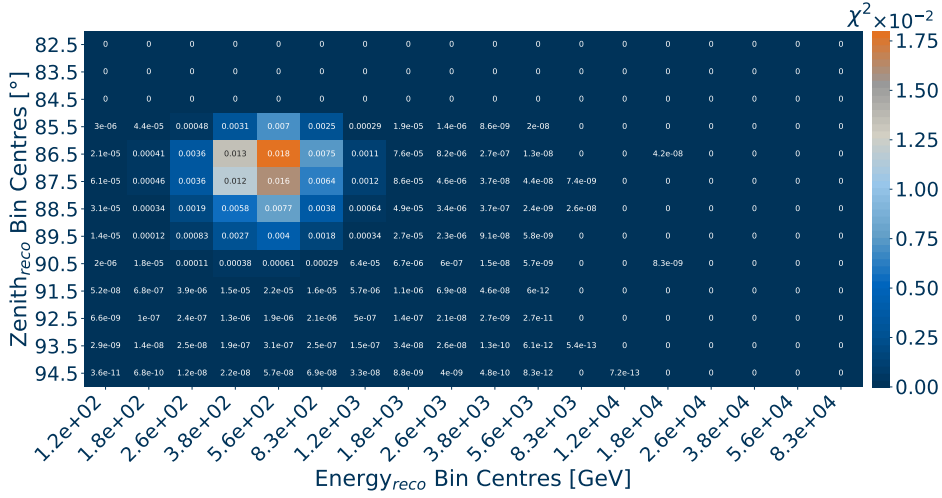


Figure 6.10: χ^2 -map for a energy/ zenith grid assuming a signal of 100 GeV staus over 1 year. χ^2 is calculated according to Equation 5.8.^{1,8}

with the time IceCube has been taking data. The topology of the χ^2 distribution over the energy/ zenith grid stays the same, while the values increase by a factor of ~ 1000 . Overall, both plots concur with the theoretical predictions and the previously shown plots.

In addition, we check the most sensitive bin from the χ^2 -map against the one with the highest rate. In this process, we recognize that when looking at the energy configuration in Figure 6.8 both bins are equal. However, in the angular view (Figure 6.9) they differ and the most sensitive bin is at a lower zenith angle than the highest rate. From both observations we are able to draw conclusions on the improvement potential discussed in chapter 8.

First however, we proceed to the calculation of our mass sensitivity for the current state of the analysis. We see from the χ^2 values in Figure 6.11, that we would be able to exclude a stau mass of 50 GeV. Already the χ^2 value of the most significant bin overcomes the threshold of 2.71 for the 90% confidence level. Though this treatment of data is correct, it is not very accurate and representative as event rates are subject to Poisson fluctuations. Hence, for a more accurate sensitivity, we use the more elaborate χ^2 measure from Equation 5.9 that incorporates 1×10^5 Poisson outcomes of signal and background distribution.

In Figure 6.12 we then depict the addressed multiplication factors from section 5.6 with respect to the assumed stau mass on the x-axis. The intersection of the curve with a multiplication factor of one marks the sensitivity for the mass limit. With our current reconstruction methods and the existing event selection, IceCube would be able to exclude stau masses < 62.9 GeV with ten years of data and neglecting systematic uncertainties.

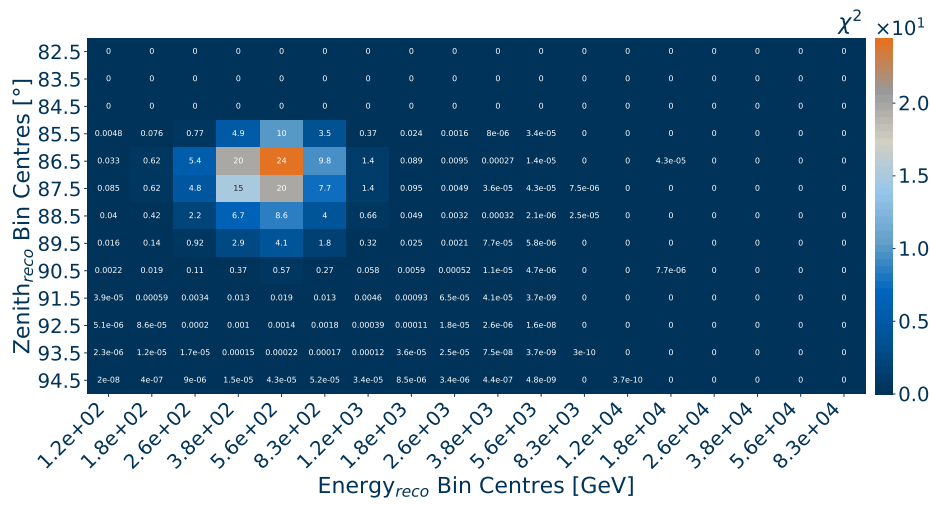


Figure 6.11: χ^2 -map for a energy/ zenith grid assuming a signal of 50 GeV staus over 10 years. χ^2 is calculated according to Equation 5.8.^{1,8}

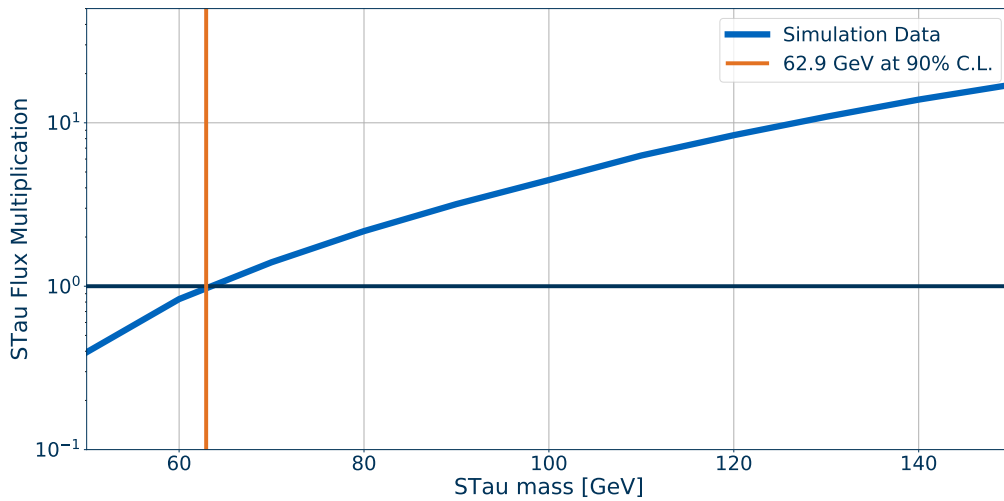


Figure 6.12: Sensitivity on the stau mass our analysis would be able to reach for 10 years of operational data, neglecting systematic uncertainties.^{1,8}

7 | CONCLUSION

In this thesis we performed a feasibility study for a novel concept to constrain BSM physics using the IceCube Neutrino Observatory. We described the theoretical fundamentals as well as the working principle of the detector and its reconstruction algorithms. With MC simulations and the application of an existing event selection, we were able to present sensitivities on the constraint of the stau mass with the current state of the analysis.

In detail, we are looking for a significant excess of low energy events in a region between 100 GeV and 1000 GeV over a remaining muon background in a region of zenith angles between 80° and 95° . The excess is thereby caused by the supersymmetric partner to the tau lepton, the stau, which is produced via Drell-Yan processes by cosmic ray interactions in the atmosphere. For our analysis, we restrict ourselves to SUSY models where the stau is a long-lived particle and is thus able to propagate to the detector after its production.

Our signature inside the detector is, due to the suppressed stochastic losses of the stau, a minimally ionizing track. Low energy muons produce similar signals in the detector and thus account for our background. However, due to the suppressed stochastic losses staus are able to penetrate further than muons, through any material. This feature defines our region of interest to incident zenith angles around the horizon. The source of the background in our region of interest comes from atmospheric muons and atmospheric neutrinos, whereat the atmospheric muons are cut out with our choice of event selection.

After our extensive study we conclude that with the current state of the analysis and neglecting systematic uncertainties, IceCube would be able to exclude the possibility of staus with masses < 62.9 GeV at 90% confidence level. This demonstrates the ability of the excess event search to constrain BSM physics, however, urges for a more elaborate implementation of the analysis. The theoretically possible limit of ~ 500 GeV is assumed to be realized for a background-free detector. In order to achieve this limit, the following chapter presents potential improvements that include for example a fitted energy estimator and event selection.

8 | OUTLOOK AND IMPROVEMENTS

Although we are not able to show a direct competitiveness with collider experiments at the current state of our analysis, we emphasize our demonstration of the feasibility and the working principle of the technique. With an unoptimized event selection and energy estimator, we obtain a sensitivity in the same order of magnitude as current limits. The current state of the analysis however, stays behind the proposed potential of the technique [1]. In the following, we thus analyze and interpret the results with respect to the future potential of the analysis. Additionally, we invoke an implementation of a partial improvement to the energy estimator.

8.1 POTENTIAL OF THE ANALYSIS

In Figure 8.1, we illustrate the ratio between the theoretical predictions from [1] and the results of our analysis. On the y-axis we show the predicted rates $R_{Prediction}$ divided by the ones obtained from our analysis $R_{Analysis}$. For better comparison, we depict this data in the same angular range between 82° and 90° as the predicted values in Figure 5.1. The ratio of the atmospheric neutrino background is marked in orange (dash-dot), whereas the difference of the stau signals is shown in blue (solid).

Looking at the comparison, we notice that for angles smaller than 85° the ratio for staus increases. Although we are not able to show data for the background ratio in that region, the overall shape of background and signal ratios are in agreement. The increase of the staus below 85° is an immediate result of the cut-off from the event selection, which suppresses the signal strength in that region. When looking at the similar shape of the curves, we see that the cut-off likely affects zenith bins above 85° as well. Namely, before we see a stabilization of the ratios above 87° , we observe increased values from 85° to 87° . A suppression of the rates by the event selection leaking into our signal region is a possible explanation for this behavior.

Another conclusion we draw from Figure 8.1 becomes evident when looking at the difference between signal and background ratios. The similar shape of the distributions is caused by the same property of the event selection. For higher angles, we see the ratio of the background approaching a value of one, indicating an accurate background estimation. When looking at the ratio of the signal, we see the same stabilizing nature of

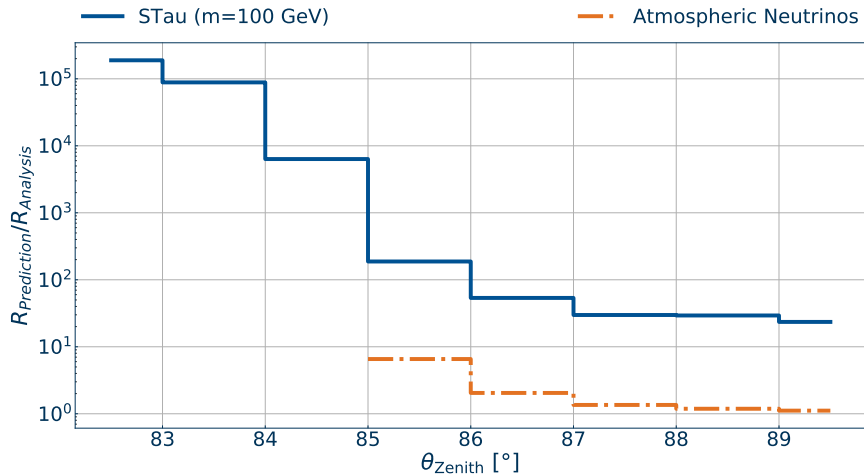


Figure 8.1: Event rate ratio for stau signal assuming a mass 100 GeV and atmospheric neutrino background with respect to the zenith angle. The difference on the y-axis is obtained by the division of the predicted data [1] over the rates calculated in this analysis.

the curve, approaching however a value > 10 . This observation hints a large potential of improvement for the stau signal acceptance.

From the comparison of the rates of our analysis to the theoretical predictions, we derive two main sources of improvement. As seen in Figure 5.1, the region of interest spans from 82° to 90° in zenith angle, with the most sensitive region being between 83° and 85° . The existing event selection used incorporates a cut below 85° in zenith angle and thus excludes the theoretically most sensitive bins. In addition, we assume from Figure 8.1 that the influence of the sharp cut-off leaks into higher zenith bins as well. This results in a lower stau rate and thus a worse signal to background ratio. Opening up the analysis to lower zenith angles resolves this issue and unlocks the full potential of our analysis with respect to the zenith range.

Another complementary improvement of the event selection targets an increased signal acceptance. In general, this leads to a higher higher stau rate and brings the analysis closer to or even further than theoretical predictions.

The extension to lower angles however, adds another source of background, that would currently dominate the exact extended region of our stau signal. Due to the misreconstruction of events to higher angles, more background events from atmospheric muons appear in our region of interest than theoretically predicted. Hence, extending the region of interest goes hand in hand with an additional background discrimination to be made.

The current analysis incorporates no active background discrimination. We use an event selection that is optimized for muon tracks and benefit that stau events mostly survive to the *Final Level* of the selection. When arranging the event selection in the other direction

and training a boosted decision tree towards our stau signal in the detector we will be able to get a better signal to background ratio. This approach will not only increase our signal acceptance but also help us to discriminate against the newly introduced background of atmospheric muons.

An additional improvement that we draw from [Figure 6.8](#) targets a better energy estimation. As we assume the distribution of the reconstructed stau energy to be a sharp peak, an improved energy estimator would resolve this peak more decisively. Similar to the event selection, an energy estimator could be trained particularly for our type of signal. This targets a more powerful energy distribution of our signal and leads to a better signal to background ratio for the most sensitive bins.

With respect to the reconstruction bias of the background that overlays with our signal, an improved energy estimator for our low energy signal might be able to eliminate this automatically. This feature adds on to the improved signal to background ratio for that the background events are more spread out. An improved energy estimator for low energy staus would thus provide two complementary benefits for the analysis.

The impact and interplay of all proposed improvements is hard to determine. In [Figure 8.1](#) however, we see that an optimized event selection might already be able to bring the analysis to the potential of the predictions. Additional improvements, for example the implicit background discrimination of a stau event selection or an improved energy estimator set free an additional potential of the analysis. Altogether, we are confident that the combination of improvements will lift the analysis to world-leading limits.

8.2 IMPROVED ENERGY ESTIMATOR

The previous section addressed and interpreted the results and derived potential sources for improvement. To test the potential of at least one proposed improvement within the scope of this thesis, we decide to use an existing energy estimator that promises to be more suitable for lower energies. This leads to a better resolution of the expected peak of the stau signal and additionally eliminates the bias for muons at low energies.

We apply the energy estimator on part of our MC stau events (2.5 million) and check its impact on our analysis. The addressed energy estimator was introduced in [112] and assigns energy values using Deep Neural Networks (DNNs). Additionally note, that the implementation of our own stau-track-optimized energy estimator, exceeds the scope of this thesis but ought to be even more powerful.

In [Figure 8.2](#) we show the energy resolution of the new energy estimator for our stau sample (top) and the DNN muon background sample used (bottom). As proposed we see the two desired effects of the energy estimator when compared to the resolution of the previous one in [Figure 6.2](#). We observe a more defined peak for the stau energies and the elimination of the low energy bias for the muons. However, we notice another effect for the muon background that we do not go into detail at this point. For now, we

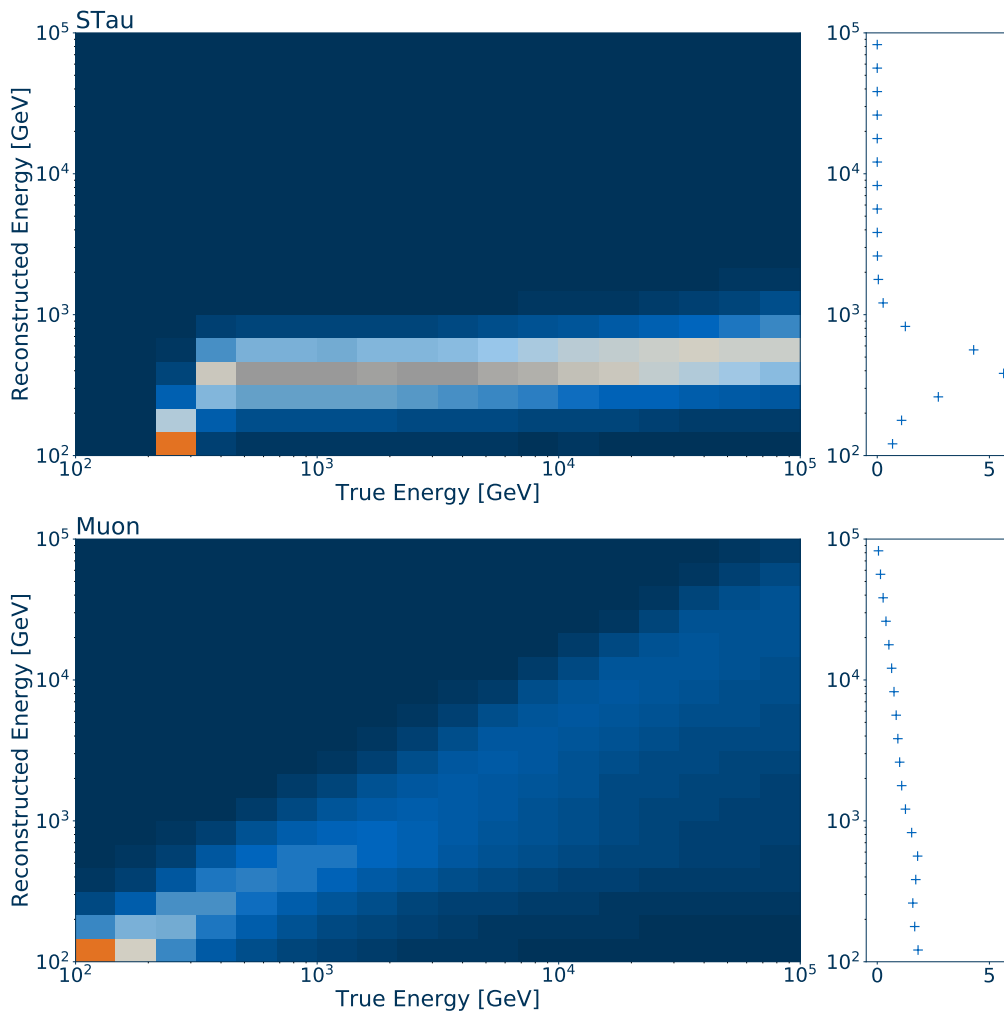


Figure 8.2: Resolution in energy for stau (top) and muon (bottom) events using the DNN energy reconstruction. The plots show a 2D histogram with the reconstructed energy on the y-axis with respect to the true MC energy on the x axis. Each column of true energy is normed with its sum of events. On the right side, we show the marginal distributions of the events, being the sum over every row.^{6,7}

just remember that the new energy estimator improves our estimation in the way we want and proceed with the steps of our analysis.

The proposed behavior becomes even more apparent when looking at the comparison of the rates in Figure 8.3. In this plot, we show the rates for a stau with mass 50 GeV and the background, similar to Figure 6.8. However, in this configuration we compare the rates of signal and background for two different energy estimators. The solid lines indicate the estimation by the standard `SplineMPE_TruncatedEnergy` estimation, while the dot-

dashed lines present the rates when applying the DNN reconstruction. We see, that not only the stau rates affirm the expectation of a more sharp and condensed peak, also the background events are shifted and more evenly distributed in our region of interest.

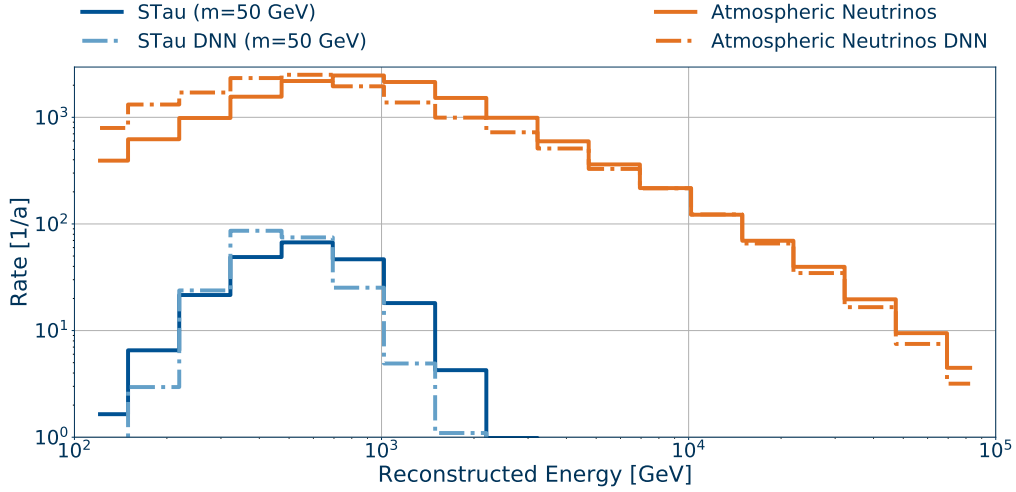


Figure 8.3: Rate comparison between 50 GeV stau mass and background for SplineMPE_TruncatedEnergy(solid) and DNN (dash-dot) energy reconstruction.^{6,7}

Now, we follow through our analysis steps and calculate the χ^2 values for each bin using the rates of our new energy estimator, assuming a 50 GeV stau mass and ten years of data. Analogous to the standard energy reconstruction with these parameters, we obtain a χ^2 map shown in Figure 8.4. We see, that the absolute values are similar to Figure 6.11, however the shape has changed and shifted to smaller energies. As expected, we see no apparent effect in angular distribution and sensitiveness for a new energy reconstruction method. For the energy distribution on the other hand, we notice a more condensed distribution of the sensitive bins. Where the significant region spanned over three to four bins in Figure 6.11, we now see a reduction to only two. Additionally, we observe a shift of the most sensitive bin to a smaller energy bin when using the improved energy reconstruction.

All of the above encourages us to calculate a mass sensitivity and see how much of an improvement we get with the DNN energy estimator. This is shown in Figure 8.5, where we present the multiplication factor necessary for the rate of staus at given mass to become a significant outcome. We show here, the old sensitivity (solid) next to the one with improved energy estimator (dash-dot) and notice an improvement of 2.2% to 64.3 GeV.

This improvement validates our theory, although it is not able to make a significant difference. In order to assess the power of this overall improvement, we have to consider that we use an existing energy estimator constructed for muons. Additionally, we use only $\sim 10\%$

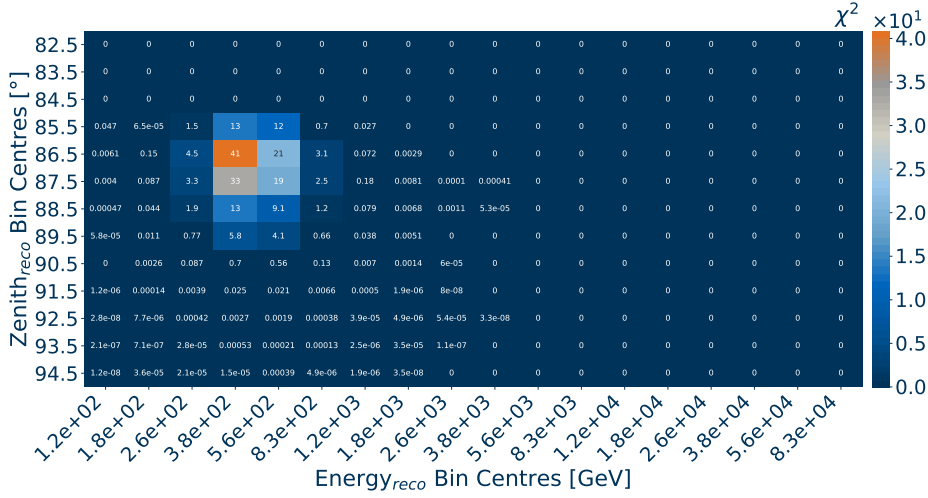


Figure 8.4: Sensitivity on the stau mass our analysis is able reach for 10 years of operational data.^{6,7}

of our available data set and therefore lack the statistical significance for a representative assessment. The latter is being addressed in the near future.

Overall, we see an improved resolution at lower energies and the elimination of the bias. This is what facilitates an improvement in the first place. A better resolution of the stau energy, leads to a more defined structure of our excess and is thus more significant. In addition, the resolution of the low energy bias for muons implicates a more flat distribution of the background and therefore a lower event count in our signal region. In Figure 8.2 however, we notice the low statistics of the stau sample in form of an unusual behavior at lower true energies and a different form of bias for the background reconstruction. Those effects likely reduce the performance of the energy estimator in terms of our analysis. In conclusion, we are able to demonstrate the potential of an improved energy estimator and emphasize that an energy estimator designed particularly for stau tracks results in a bigger leap in the sensitivity.

8.3 IMPROVEMENTS OUTSIDE THE ANALYSIS

Our feasibility study demonstrates an alternative to collider experiments in order to constrain the physics of heavy, charged, long-lived BSM particles using existing neutrino telescopes. The almost model-independent approach enables the search for a large range of particles, similar to the stau. In addition, the analysis is not limited to ice as a target material but is applicable in water-based telescopes as well. The model independence and the unrestricted application in all neutrino telescope facilitates many combinations of searches. A combined analysis of these searches would have a great opportunity to exceed the limits of collider experiments.

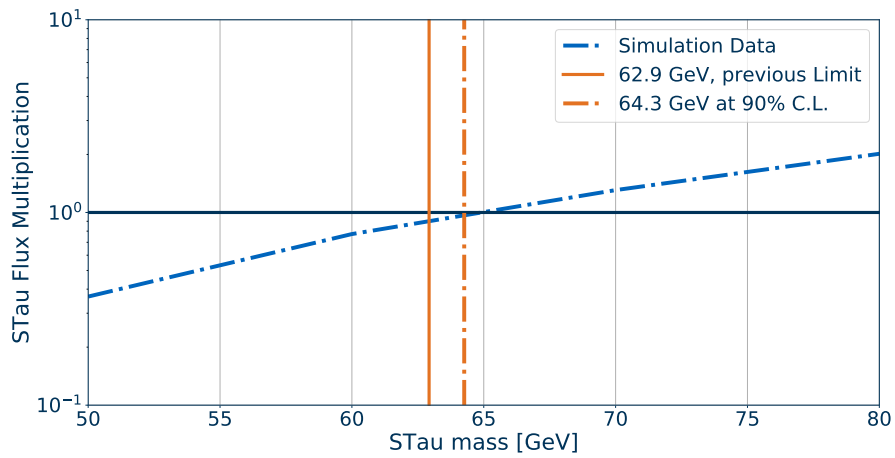


Figure 8.5: Improved sensitivity on the stau mass our analysis would be able to reach for 10 years of operational data, neglecting systematic uncertainties and using the DNN energy estimator.^{6,7}

Furthermore, the improvement or development of new large scale neutrino telescopes, such as IceCube-Gen2 [113], P-ONE [114], KM3NET [115] and Baikal-GVD [116] promises great prospects for neutrino astronomy. However, any improvement of a telescope targeting a larger volume, a better reconstruction at low energies is expected to further improve our analysis as well.

A | SUPPLEMENTARY MATERIAL

A.1 MC SAMPLES AND CUTS

- ¹ using the remaining events on *Final Level* from a sample of 20 million stau events.
- ² using the remaining events on *Final Level* from a sample of 500 thousand muon events.
- ³ using the remaining events on each level (*Generation, Trigger, Level2, Final Level*) starting with a MC sample of 500 thousand events.
- ⁴ using only events with a simulated zenith angle between $85^\circ - 105^\circ$
- ⁵ using only events with a reconstructed energy between 100 GeV-1000 GeV
- ⁶ using the remaining events on *Final Level* from a sample of 2.5 million stau events with DNN energy reconstruction
- ⁷ using the remaining events on *Final Level* from the simulated background sample in [112] with DNN energy reconstruction
- ⁸ using the remaining events on *Final Level* from the simulated background sample in [104]

A.2 NLSP CONDITION AND STAU MASS MATRIX

The equation is only referred to for the completeness and will not be part of a fundamental discussion as this is not relevant for the topic of this thesis. A detailed derivation and explanation can be found in the reference.

$$N > \frac{66}{5(13\xi_1 - 2)}, \quad \xi_1 \equiv \frac{\alpha_1^2(M_1)}{\alpha_1^2(M)} = \left[1 + \frac{11}{4\pi}\alpha_1(M_1)\ln\frac{M_1^2}{M^2}\right]^2. \quad (\text{A.1})$$

Hereby M_1 corresponds to the Bino-mass, N is the messenger index defined in [26] and M represents the mass scale of supersymmetry breaking. A combination of moderate values for N and small M (e.g. $N = 1.7$ for $M = 10^5$ GeV) enables the change of the NLSP from neutralino to stau. Large M (10^{12} GeV) however, also require a large N (>5) for the stau to be long-lived. For a higher mixing $\tan\beta$, the stau can be the NLSP for even smaller N in Equation A.1.

The stau mass matrix according to [26] is:

$$m_{\tilde{\tau}}^2 = \begin{pmatrix} m_{\tilde{L}_L}^2 + m_{\tilde{\tau}}^2 - (\frac{1}{2} - \sin^2 \theta_W) \cos 2\beta M_Z^2 & m_{\tilde{\tau}}(A_{\tilde{\tau}} - \mu \tan \beta) \\ m_{\tilde{\tau}}(A_{\tilde{\tau}} - \mu \tan \beta) & m_{\tilde{E}_R}^2 + m_{\tilde{\tau}}^2 - \sin^2 \theta_W \cos 2\beta M_Z^2 \end{pmatrix}. \quad (\text{A.2})$$

A.3 PARAMETERS CR MODEL

The following table lists the cut-offs R_c , the power law indices $\gamma_{i,j}$ and normalization constants $a_{i,j}$ for Equation 3.1. The values are taken from [56].

Origin j	R_c	γ	p	He	CNO	Mg-Si	Fe
γ for $j = 1$	-	-	1.66	1.58	1.63	1.67	1.63
$j = 1$	4 PeV	see line 1	7860	3550	2200	1430	2120
$j = 2$	30 PeV	1.4	20	20	13.4	13.4	13.4
$j = 3$	2 EeV	1.4	1.7	1.7	1.14	1.14	1.14
protons only	60 EeV	1.6	200	0	0	0	0

A.4 TRAVEL LENGTH SIMULATION IN ICE

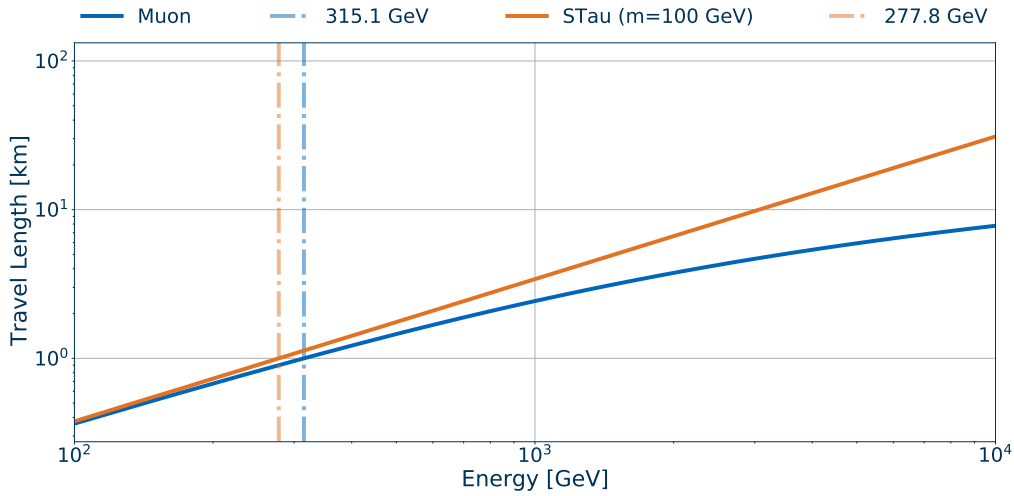


Figure A.1: Comparison of the travel length in ice with respect to the initial energy for muons and staus ($m=100$ GeV). For the simulation we assume an energy loss according to Equation 2.3 with data from [40].

LIST OF FIGURES

2.1	The Standard Model particles and their supersymmetric counterparts. [16] Note that this is the depiction of one model using SUSY and that not every model necessarily includes these particle. he focus in this thesis lies on the supersymmetric partner of the tau lepton, displayed in this picture as the second from the top right corner, the stau.	4
2.2	Feynman diagram of a Drell-Yan process on the production of staus in our analysis. In our case, the two outgoing leptons are a pair of staus $\tilde{\tau}$	7
2.3	Stau mass dependence of the cross section for the stau production at proton-proton collisions. Displayed is the data of two different beam energies simulated by MadGraph [34]. Note, that the displayed cross sections are tree-level data. For higher orders and corrections see [37].	8
2.4	Comparison between the energy loss of a stau and a muon in ice, using Equation 2.3 and [40] for values of a and b	9
3.1	Two different representations of the Cosmic Ray spectrum proportional to the energy of the incident particle. The plot on the top includes proton-only measurements for the range below 100 TeV, whereas the bottom plot is restricted to all-particle measurements. In the first graph, the flux is multiplied by the particles energy, which is a common way to depict the event rates, as energy measurements usually have a precision δE , proportional to the energy [46]. In order to enhance the features of the spectrum the flux is usually multiplied by the energy to a higher order (here 2.7). The representation of that is shown in the second graph. Data was taken from [47–54]	12
3.2	Schematic of an atmospheric particle cascade. A CR primary hits the top of the atmosphere and triggers a chain of other particle interactions. What percentage of particles arrives on the surface of the earth depends mainly on the properties of the primary.	16
3.3	Multi-Messenger Astronomy [70]	19
4.1	Schematic representation of the IceCube Neutrino Observatory at the South Pole including a depiction of the precursor AMANDA	23
4.2	Energy deposition inside the detector of a muon and a 100 GeV stau. With the data of the energy loss in Figure 2.4, we calculate the deposition of the particle when traversing the detector (1 km of ice).	26

4.3	Depiction of a MC stau event in the IceCube detector. The stau was initialized with an energy of 23 TeV at a zenith angle of 88.7° and has been reconstructed to 573 GeV with a direction of 88.5° in zenith.	27
5.1	Predicted number of stau and muon events in IceCube per year as a function of the arrival direction in form of the zenith angle. The data was courteously provided by [1]. For the stau events a pure Drell-Yan production and masses of 100 and 200 GeV have been assumed, dark and light blue respectively. The muon events are shown separately and divided in their contribution from hadronic interactions (gray, dashed) and from neutrino interactions (orange, dash-dot). The shaded regions of each curve show the model uncertainties.	30
5.2	The flux of staus at the IceCube detector for three different directions in zenith angle assuming a mass of 100 GeV.	31
5.3	Depiction of the propagation of Cherenkov photons emerging from a charged particle traveling through a medium. As an example we show two DOM modules that capture the Cherenkov light at different times, depending among other things on the geometry of the track and the optical ice properties.	33
5.4	Approximation of the different materials passed in the way to the detector in relation to the zenith angle. The representation is based on the assumption of 80 km of atmosphere surrounding the earth covered with a 3.5 km layer of ice/water.	36
6.1	Resolution in zenith angle for stau and muon events using the <code>SplineMPE</code> reconstruction (section 5.3). The bars represent the 68% region around the median (orange). No stau events are reconstructed in the first energy bin, hence no bar can be displayed. ^{1,2}	44
6.2	Resolution in energy for stau (top) and muon (bottom) events using the <code>SplineMPE_TruncatedEnergy</code> reconstruction (section 5.3). The plots show a 2D histogram with the reconstructed energy on the y-axis with respect to the true MC energy on the x axis. Each column of true energy is normed with its sum of events. On the right side, we show the marginal distributions of the events, being the sum over every row. ^{1,2}	45
6.3	Effective area of muon events at different levels of the event selection. ^{3,4}	46
6.4	Effective area of stau events at different levels of the event selection. ^{3,4}	47
6.5	Effective area of stau and muon events. ^{1,2,4}	48
6.6	Effective area of stau events at <i>Final Level</i> for three specific zenith bins (85° , 90° and 95°). ^{1,4}	48
6.7	3D representation of the stau rates on a energy/ zenith binned grid with integrated rates over energy and angle on the respective x-z and y-z plane. ¹	49
6.8	Event rates of staus for masses of 50 GeV and 100 GeV and the atmospheric neutrino background integrated over angles from 80° to 95° zenith. ^{1,8}	50
6.9	Event rates of staus for masses of 50 GeV and 100 GeV and the atmospheric neutrino background. ^{1,5,8}	51
6.10	χ^2 -map for a energy/ zenith grid assuming a signal of 100 GeV staus over 1 year. χ^2 is calculated according to Equation 5.8. ^{1,8}	52
6.11	χ^2 -map for a energy/ zenith grid assuming a signal of 50 GeV staus over 10 years. χ^2 is calculated according to Equation 5.8. ^{1,8}	53

6.12	Sensitivity on the stau mass our analysis would be able to reach for 10 years of operational data, neglecting systematic uncertainties. ^{1,8}	53
8.1	Event rate ratio for stau signal assuming a mass 100 GeV and atmospheric neutrino background with respect to the zenith angle. The difference on the y-axis is obtained by the division of the predicted data [1] over the rates calculated in this analysis.	58
8.2	Resolution in energy for stau (top) and muon (bottom) events using the DNN energy reconstruction. The plots show a 2D histogram with the reconstructed energy on the y-axis with respect to the true MC energy on the x axis. Each column of true energy is normed with its sum of events. On the right side, we show the marginal distributions of the events, being the sum over every row. ^{6,7}	60
8.3	Rate comparison between 50 GeV stau mass and background for SplineMPE_TruncatedEnergy(solid) and DNN (dash-dot) energy reconstruction. ^{6,7}	61
8.4	Sensitivity on the stau mass our analysis is able reach for 10 years of operational data. ^{6,7}	62
8.5	Improved sensitivity on the stau mass our analysis would be able to reach for 10 years of operational data, neglecting systematic uncertainties and using the DNN energy estimator. ^{6,7}	63
A.1	Comparison of the travel length in ice with respect to the initial energy for muons and staus ($m=100$ GeV). For the simulation we assume an energy loss according to Equation 2.3 with data from [40].	66

BIBLIOGRAPHY

- [1] Stephan Meighen-Berger et al. 'New constraints on supersymmetry using neutrino telescopes'. In: *Phys. Lett. B* 811 (2020), p. 135929. DOI: 10.1016/j.physletb.2020.135929. arXiv: 2005.07523 [hep-ph].
- [2] S. L. Glashow. 'Partial Symmetries of Weak Interactions'. In: *Nucl. Phys.* 22 (1961), pp. 579–588. DOI: 10.1016/0029-5582(61)90469-2.
- [3] Peter W. Higgs. 'Broken Symmetries and the Masses of Gauge Bosons'. In: *Phys. Rev. Lett.* 13 (1964). Ed. by J. C. Taylor, pp. 508–509. DOI: 10.1103/PhysRevLett.13.508.
- [4] Murray Gell-Mann. 'A Schematic Model of Baryons and Mesons'. In: *Phys. Lett.* 8 (1964), pp. 214–215. DOI: 10.1016/S0031-9163(64)92001-3.
- [5] G. Zweig. 'An SU(3) model for strong interaction symmetry and its breaking. Version 2'. In: *DEVELOPMENTS IN THE QUARK THEORY OF HADRONS. VOL. 1. 1964 - 1978*. Ed. by D. B. Lichtenberg and Simon Peter Rosen. Feb. 1964.
- [6] Steven Weinberg. 'A Model of Leptons'. In: *Phys. Rev. Lett.* 19 (1967), pp. 1264–1266. DOI: 10.1103/PhysRevLett.19.1264.
- [7] Abdus Salam. 'Weak and Electromagnetic Interactions'. In: *Conf. Proc. C* 680519 (1968), pp. 367–377. DOI: 10.1142/9789812795915_0034.
- [8] F. Zwicky. 'Die Rotverschiebung von extragalaktischen Nebeln'. In: *Helv. Phys. Acta* 6 (1933), pp. 110–127. DOI: 10.1007/s10714-008-0707-4.
- [9] P. A. R. Ade et al. 'Planck 2015 results. XIII. Cosmological parameters'. In: *Astron. Astrophys.* 594 (2016), A13. DOI: 10.1051/0004-6361/201525830. arXiv: 1502.01589 [astro-ph.CO].
- [10] Peter Minkowski. ' $\mu \rightarrow e\gamma$ at a Rate of One Out of 10^9 Muon Decays?'. In: *Phys. Lett. B* 67 (1977), pp. 421–428. DOI: 10.1016/0370-2693(77)90435-X.
- [11] Tsutomu Yanagida. 'Horizontal Symmetry and Masses of Neutrinos'. In: *Prog. Theor. Phys.* 64 (1980), p. 1103. DOI: 10.1143/PTP.64.1103.
- [12] Mordehai Milgrom. 'Dynamics with a non-standard inertia-acceleration relation: an alternative to dark matter'. In: *Annals Phys.* 229 (1994), pp. 384–415. DOI: 10.1006/aphy.1994.1012. arXiv: astro-ph/9303012.

- [13] Jacob D. Bekenstein. 'Relativistic gravitation theory for the MOND paradigm'. In: *Phys. Rev. D* 70 (2004). [Erratum: *Phys.Rev.D* 71, 069901 (2005)], p. 083509. DOI: 10.1103/PhysRevD.70.083509. arXiv: astro-ph/0403694.
- [14] P. A. Zyla et al. 'Review of Particle Physics'. In: *PTEP* 2020.8 (2020), p. 083C01. DOI: 10.1093/ptep/ptaa104.
- [15] T Morii, C S Lim and S N Mukherjee. *The Physics of the Standard Model and Beyond*. WORLD SCIENTIFIC, 2004. DOI: 10.1142/4655. eprint: <https://www.worldscientific.com/doi/pdf/10.1142/4655>. URL: <https://www.worldscientific.com/doi/abs/10.1142/4655>.
- [16] C. David. *The Standard Model particles and their supersymmetric counterparts*.
- [17] Howard E. Haber and Laurel Stephenson Haskins. 'Supersymmetric Theory and Models'. In: *Anticipating the Next Discoveries in Particle Physics* (May 2018). DOI: 10.1142/9789813233348_0006. URL: http://dx.doi.org/10.1142/9789813233348_0006.
- [18] Ivone Albuquerque, Gustavo Burdman and Z. Chacko. 'Neutrino telescopes as a direct probe of supersymmetry breaking'. In: *Phys. Rev. Lett.* 92 (2004), p. 221802. DOI: 10.1103/PhysRevLett.92.221802. arXiv: hep-ph/0312197.
- [19] Markus Ahlers, Jörn Kersten and Andreas Ringwald. 'Long-lived staus at neutrino telescopes'. In: *JCAP* 07 (2006), p. 005. DOI: 10.1088/1475-7516/2006/07/005. arXiv: hep-ph/0604188.
- [20] L. Girardello and Marcus T. Grisaru. 'Soft Breaking of Supersymmetry'. In: *Nucl. Phys. B* 194 (1982), p. 65. DOI: 10.1016/0550-3213(82)90512-0.
- [21] Savas Dimopoulos and Howard Georgi. 'Softly Broken Supersymmetry and SU(5)'. In: *Nucl. Phys. B* 193 (1981), pp. 150–162. DOI: 10.1016/0550-3213(81)90522-8.
- [22] N. Sakai. 'Naturalness in Supersymmetric Guts'. In: *Z. Phys. C* 11 (1981), p. 153. DOI: 10.1007/BF01573998.
- [23] Pierre Fayet. 'Spontaneously Broken Supersymmetric Theories of Weak, Electromagnetic and Strong Interactions'. In: *Phys. Lett. B* 69 (1977), p. 489. DOI: 10.1016/0370-2693(77)90852-8.
- [24] Claire Anne Sophie David. 'Search for Supersymmetry using a Higgs boson in the decay cascade with the ATLAS detector at the Large Hadron Collider'. PhD thesis. Victoria U., Apr. 2016.
- [25] Savas Dimopoulos and David W. Sutter. 'The Supersymmetric flavor problem'. In: *Nucl. Phys. B* 452 (1995), pp. 496–512. DOI: 10.1016/0550-3213(95)00421-N. arXiv: hep-ph/9504415.
- [26] G. F. Giudice and R. Rattazzi. 'Theories with gauge mediated supersymmetry breaking'. In: *Phys. Rept.* 322 (1999), pp. 419–499. DOI: 10.1016/S0370-1573(99)00042-3. arXiv: hep-ph/9801271.

- [27] Grigoris Panotopoulos. ‘Supersymmetric dark matter, catalyzed BBN, and heavy moduli in mSUGRA with gravitino LSP and stau NLSP’. In: *Physics Letters B* 671.3 (2009), pp. 327–330. ISSN: 0370-2693. DOI: <https://doi.org/10.1016/j.physletb.2008.12.047>. URL: <https://www.sciencedirect.com/science/article/pii/S0370269308015438>.
- [28] Josef Pradler and Frank Daniel Steffen. ‘Implications of catalyzed BBN in the CMSSM with gravitino dark matter’. In: *Physics Letters B* 666.2 (Aug. 2008), pp. 181–184. ISSN: 0370-2693. DOI: 10.1016/j.physletb.2008.07.050. URL: <http://dx.doi.org/10.1016/j.physletb.2008.07.050>.
- [29] Leszek Roszkowski, Roberto Ruiz de Austri and Ki-Young Choi. ‘Gravitino dark matter in the CMSSM and implications for leptogenesis and the LHC’. In: *Journal of High Energy Physics* 2005.08 (Aug. 2005), pp. 080–080. ISSN: 1029-8479. DOI: 10.1088/1126-6708/2005/08/080. URL: <http://dx.doi.org/10.1088/1126-6708/2005/08/080>.
- [30] Jonathan L. Feng, Shufang Su and Fumihiro Takayama. ‘Supergravity with a gravitino lightest supersymmetric particle’. In: *Physical Review D* 70.7 (Oct. 2004). ISSN: 1550-2368. DOI: 10.1103/physrevd.70.075019. URL: <http://dx.doi.org/10.1103/PhysRevD.70.075019>.
- [31] A. Bartl et al. ‘Production of stop, sbottom, and stau at LEP2’. In: *Zeitschrift für Physik C Particles and Fields* 73.3 (Feb. 1997), pp. 469–476. ISSN: 1431-5858. DOI: 10.1007/s002880050337. URL: <http://dx.doi.org/10.1007/s002880050337>.
- [32] Sidney D. Drell and Tung-Mow Yan. ‘Massive Lepton-Pair Production in Hadron-Hadron Collisions at High Energies’. In: *Phys. Rev. Lett.* 25 (13 Sept. 1970), pp. 902–902. DOI: 10.1103/PhysRevLett.25.902.2. URL: <https://link.aps.org/doi/10.1103/PhysRevLett.25.902.2>.
- [33] Jan Heisig and Jörn Kersten. ‘Production of long-lived staus in the Drell-Yan process’. In: *Phys. Rev. D* 84 (2011), p. 115009. DOI: 10.1103/PhysRevD.84.115009. arXiv: 1106.0764 [hep-ph].
- [34] J. Alwall et al. ‘The automated computation of tree-level and next-to-leading order differential cross sections, and their matching to parton shower simulations’. In: *Journal of High Energy Physics* 2014.7 (July 2014). ISSN: 1029-8479. DOI: 10.1007/jhep07(2014)079. URL: [http://dx.doi.org/10.1007/JHEP07\(2014\)079](http://dx.doi.org/10.1007/JHEP07(2014)079).
- [35] R. J. Glauber and G. Matthiae. ‘High-energy scattering of protons by nuclei’. In: *Nucl. Phys. B* 21 (1970), pp. 135–157. DOI: 10.1016/0550-3213(70)90511-0.
- [36] T. Wibig and D. Sobczynska. ‘Proton - nucleus cross-section at high-energies’. In: *J. Phys. G* 24 (1998), pp. 2037–2047. DOI: 10.1088/0954-3899/24/11/006. arXiv: hep-ph/9809494.
- [37] Jonas M. Lindert, Frank D. Steffen and Maike K. Trenkel. *Direct stau production at the LHC*. 2012. arXiv: 1204.2379 [hep-ph].

- [38] Stephan Meighen-Berger. ‘Precision background modeling for neutrino telescopes’. PhD thesis. Munich, Tech. U., 2021.
- [39] M. H. Reno, I. Sarcevic and S. Su. ‘Propagation of supersymmetric charged sleptons at high energies’. In: *Astropart. Phys.* 24 (2005), pp. 107–115. DOI: 10.1016/j.astropartphys.2005.06.002. arXiv: hep-ph/0503030.
- [40] Donald E. Groom, Nikolai V. Mokhov and Sergei I. Striganov. ‘Muon stopping power and range tables 10-MeV to 100-TeV’. In: *Atom. Data Nucl. Data Tabl.* 78 (2001), pp. 183–356. DOI: 10.1006/adnd.2001.0861.
- [41] Morad Aaboud et al. ‘Search for heavy charged long-lived particles in the ATLAS detector in 36.1 fb^{-1} of proton-proton collision data at $\sqrt{s} = 13 \text{ TeV}$ ’. In: *Phys. Rev. D* 99.9 (2019), p. 092007. DOI: 10.1103/PhysRevD.99.092007. arXiv: 1902.01636 [hep-ex].
- [42] Markus Ahlers, Jörn Kersten and Andreas Ringwald. ‘Long-lived staus at neutrino telescopes’. In: *JCAP* 07 (2006), p. 005. DOI: 10.1088/1475-7516/2006/07/005. arXiv: hep-ph/0604188.
- [43] Sandro Kopper. ‘Search for Exotic Double Tracks with the IceCube Neutrino Telescope’. PhD thesis. Wuppertal U., 2016.
- [44] R. Abbasi et al. ‘Lateral Distribution of Muons in IceCube Cosmic Ray Events’. In: *Phys. Rev. D* 87.1 (2013), p. 012005. DOI: 10.1103/PhysRevD.87.012005. arXiv: 1208.2979 [astro-ph.HE].
- [45] Victor F. Hess. ‘Über Beobachtungen der durchdringenden Strahlung bei sieben Freiballonfahrten’. In: *Phys. Z.* 13 (1912), pp. 1084–1091.
- [46] Thomas K. Gaisser, Ralph Engel and Elisa Resconi. *Cosmic Rays and Particle Physics: 2nd Edition*. Cambridge University Press, June 2016. ISBN: 978-0-521-01646-9.
- [47] M. Aguilar et al. ‘Precision Measurement of the Proton Flux in Primary Cosmic Rays from Rigidity 1 GV to 1.8 TV with the Alpha Magnetic Spectrometer on the International Space Station’. In: *Phys. Rev. Lett.* 114 (2015), p. 171103. DOI: 10.1103/PhysRevLett.114.171103.
- [48] Y. S. Yoon et al. ‘Proton and Helium Spectra from the CREAM-III Flight’. In: *Astrophys. J.* 839.1 (2017), p. 5. DOI: 10.3847/1538-4357/aa68e4. arXiv: 1704.02512 [astro-ph.HE].
- [49] M. G. Aartsen et al. ‘Measurement of the cosmic ray energy spectrum with IceTop-73’. In: *Phys. Rev. D* 88.4 (2013), p. 042004. DOI: 10.1103/PhysRevD.88.042004. arXiv: 1307.3795 [astro-ph.HE].
- [50] W. D. Apel et al. ‘The spectrum of high-energy cosmic rays measured with KASCADE-Grande’. In: *Astropart. Phys.* 36 (2012), pp. 183–194. DOI: 10.1016/j.astropartphys.2012.05.023.

- [51] M. Amenomori et al. 'The All-particle spectrum of primary cosmic rays in the wide energy range from 10^{14} eV to 10^{17} eV observed with the Tibet-III air-shower array'. In: *Astrophys. J.* 678 (2008), pp. 1165–1179. DOI: 10.1086/529514. arXiv: 0801.1803 [hep-ex].
- [52] R. U. Abbasi et al. 'First observation of the Greisen-Zatsepin-Kuzmin suppression'. In: *Phys. Rev. Lett.* 100 (2008), p. 101101. DOI: 10.1103/PhysRevLett.100.101101. arXiv: astro-ph/0703099.
- [53] Francesco Fenu. 'The cosmic ray energy spectrum measured using the Pierre Auger Observatory'. In: *PoS ICRC2017* (2018). Ed. by Darko Veberic, p. 486. DOI: 10.22323/1.301.0486.
- [54] Yoshiki Tsunesada et al. 'Energy Spectrum of Ultra-High-Energy Cosmic Rays Measured by The Telescope Array'. In: *PoS ICRC2017* (2018), p. 535. DOI: 10.22323/1.301.0535.
- [55] Matthias Huber. 'Multi-Messenger correlation study of Fermi-LAT blazars and high-energy neutrinos observed in IceCube'. PhD thesis. Munich, Tech. U., 2020. URL: https://www.groups.ph.tum.de/fileadmin/w00bya/cosmic-particles/Thesis/phd_hubi.pdf (visited on 18/04/2021).
- [56] Thomas K. Gaisser. 'Spectrum of cosmic-ray nucleons, kaon production, and the atmospheric muon charge ratio'. In: *Astropart. Phys.* 35 (2012), pp. 801–806. DOI: 10.1016/j.astropartphys.2012.02.010. arXiv: 1111.6675 [astro-ph.HE].
- [57] Joerg R. Hoerandel. 'On the knee in the energy spectrum of cosmic rays'. In: *Astropart. Phys.* 19 (2003), pp. 193–220. DOI: 10.1016/S0927-6505(02)00198-6. arXiv: astro-ph/0210453.
- [58] B. Peters. 'Primary cosmic radiation and extensive air showers'. In: *Il Nuovo Cimento (1955-1965)* 22 (4 Nov. 1961), pp. 800–819. DOI: <https://doi.org/10.1007/BF02783106>.
- [59] Johannes Blumer, Ralph Engel and Jorg R. Horandel. 'Cosmic Rays from the Knee to the Highest Energies'. In: *Prog. Part. Nucl. Phys.* 63 (2009), pp. 293–338. DOI: 10.1016/j.pnpnp.2009.05.002. arXiv: 0904.0725 [astro-ph.HE].
- [60] Karl-Heinz Kampert and Peter Tinyakov. 'Cosmic rays from the ankle to the cutoff'. In: *Comptes Rendus Physique* 15 (2014), pp. 318–328. DOI: 10.1016/j.crhy.2014.04.006. arXiv: 1405.0575 [astro-ph.HE].
- [61] A. M. Hillas. 'The Origin of Ultra-High-Energy Cosmic Rays'. In: *Annual Review of Astronomy and Astrophysics* 22.1 (1984), pp. 425–444. DOI: 10.1146/annurev.aa.22.090184.002233. eprint: <https://doi.org/10.1146/annurev.aa.22.090184.002233>. URL: <https://doi.org/10.1146/annurev.aa.22.090184.002233>.
- [62] Kenneth Greisen. 'End to the cosmic ray spectrum?' In: *Phys. Rev. Lett.* 16 (1966), pp. 748–750. DOI: 10.1103/PhysRevLett.16.748.

- [63] G. T. Zatsepin and V. A. Kuzmin. ‘Upper limit of the spectrum of cosmic rays’. In: *JETP Lett.* 4 (1966), pp. 78–80.
- [64] T. Abu-Zayyad et al. ‘The Cosmic Ray Energy Spectrum Observed with the Surface Detector of the Telescope Array Experiment’. In: *Astrophys. J. Lett.* 768 (2013), p. L1. DOI: 10.1088/2041-8205/768/1/L1. arXiv: 1205.5067 [astro-ph.HE].
- [65] Alexander Aab et al. ‘Evidence for a mixed mass composition at the ‘ankle’ in the cosmic-ray spectrum’. In: *Phys. Lett. B* 762 (2016), pp. 288–295. DOI: 10.1016/j.physletb.2016.09.039. arXiv: 1609.08567 [astro-ph.HE].
- [66] Valerio Verzi, Dmitri Ivanov and Yoshiki Tsunesada. ‘Measurement of Energy Spectrum of Ultra-High Energy Cosmic Rays’. In: *PTEP* 2017.12 (2017), 12A103. DOI: 10.1093/ptep/ptx082. arXiv: 1705.09111 [astro-ph.HE].
- [67] Jürgen Brunner. ‘Measurement of Neutrino Oscillations with Neutrino Telescopes’. In: *Adv. High Energy Phys.* 2013 (2013), p. 782538. DOI: 10.1155/2013/782538.
- [68] Soebur Razzaque, Olga Mena and Irina Mocioiu. ‘Determination of Neutrino Mass Hierarchy from the Deep Core Extension of the IceCube data on Atmospheric Neutrinos’. In: *APS April Meeting Abstracts*. APS Meeting Abstracts. May 2009, E1.043.
- [69] D. Heck et al. ‘CORSIKA: A Monte Carlo code to simulate extensive air showers’. In: (Feb. 1998).
- [70] The IceCube Collaboration. *IceCube Multi-Messenger Propagation*. 2018. URL: <https://gallery.icecube.wisc.edu/internal/d/318865-1/physicus.pdf> (visited on 15/05/2021).
- [71] I.A. Belolaptikov et al. ‘The Baikal underwater neutrino telescope: Design, performance, and first results’. In: *Astroparticle Physics* 7.3 (1997), pp. 263–282. ISSN: 0927-6505. DOI: [https://doi.org/10.1016/S0927-6505\(97\)00022-4](https://doi.org/10.1016/S0927-6505(97)00022-4). URL: <https://www.sciencedirect.com/science/article/pii/S0927650597000224>.
- [72] E. Andres et al. ‘The AMANDA neutrino telescope: principle of operation and first results’. In: *Astroparticle Physics* 13.1 (2000), pp. 1–20. ISSN: 0927-6505. DOI: [https://doi.org/10.1016/S0927-6505\(99\)00092-4](https://doi.org/10.1016/S0927-6505(99)00092-4). URL: <https://www.sciencedirect.com/science/article/pii/S0927650599000924>.
- [73] M. Ageron et al. ‘ANTARES: The first undersea neutrino telescope’. In: *Nuclear Instruments and Methods in Physics Research Section A: Accelerators, Spectrometers, Detectors and Associated Equipment* 656.1 (2011), pp. 11–38. ISSN: 0168-9002. DOI: <https://doi.org/10.1016/j.nima.2011.06.103>. URL: <https://www.sciencedirect.com/science/article/pii/S0168900211013994>.
- [74] Eli Waxman and John N. Bahcall. ‘High-energy neutrinos from astrophysical sources: An Upper bound’. In: *Phys. Rev. D* 59 (1999), p. 023002. DOI: 10.1103/PhysRevD.59.023002. arXiv: hep-ph/9807282.

- [75] B. P. Abbott et al. ‘Multi-messenger Observations of a Binary Neutron Star Merger’. In: *Astrophys. J. Lett.* 848.2 (2017), p. L12. DOI: 10.3847/2041-8213/aa91c9. arXiv: 1710.05833 [astro-ph.HE].
- [76] M. G. Aartsen et al. ‘Multimessenger observations of a flaring blazar coincident with high-energy neutrino IceCube-170922A’. In: *Science* 361.6398 (2018), eaat1378. DOI: 10.1126/science.aat1378. arXiv: 1807.08816 [astro-ph.HE].
- [77] M. G. Aartsen et al. ‘The IceCube Neutrino Observatory: Instrumentation and Online Systems’. In: *JINST* 12.03 (2017), P03012. DOI: 10.1088/1748-0221/12/03/P03012. arXiv: 1612.05093 [astro-ph.IM].
- [78] P. A. Čerenkov. ‘Visible Radiation Produced by Electrons Moving in a Medium with Velocities Exceeding that of Light’. In: *Phys. Rev.* 52 (4 Aug. 1937), pp. 378–379. DOI: 10.1103/PhysRev.52.378. URL: <https://link.aps.org/doi/10.1103/PhysRev.52.378>.
- [79] I. M. Frank and I. E. Tamm. ‘Coherent visible radiation of fast electrons passing through matter’. In: *Compt. Rend. Acad. Sci. URSS* 14.3 (1937), pp. 109–114. DOI: 10.3367/UFNr.0093.196710o.0388.
- [80] F. Kulcsár, D. Teherani and H. Altmann. ‘Study of the spectrum of cherenkov light’. In: *Journal of radioanalytical chemistry* 68 (1 Mar. 1982), pp. 161–168. DOI: 10.1007/BF02517618. URL: <https://doi.org/10.1007/BF02517618>.
- [81] J. V. Jelley. ‘Čerenkov radiation: Its origin, properties and applications’. In: *Contemporary Physics* 3.1 (1961), pp. 45–57. DOI: 10.1080/00107516108204445. eprint: <https://doi.org/10.1080/00107516108204445>. URL: <https://doi.org/10.1080/00107516108204445>.
- [82] The IceCube Collaboration. *Layered Scattering and Absorption Coefficients in Spice 3.2.1*. 2018. URL: https://wiki.icecube.wisc.edu/index.php/File:Spice3.2.1_layered_scatt_abs_withlength.png (visited on 05/06/2021).
- [83] P. A. Zyla et al. ‘Review of Particle Physics’. In: *PTEP* 2020.8 (2020), p. 083C01. DOI: 10.1093/ptep/ptaa104.
- [84] L. Wan et al. ‘Measurement of the neutrino-oxygen neutral-current quasielastic cross section using atmospheric neutrinos at Super-Kamiokande’. In: *Phys. Rev. D* 99.3 (2019), p. 032005. DOI: 10.1103/PhysRevD.99.032005. arXiv: 1901.05281 [hep-ex].
- [85] R. Abbasi et al. ‘IceCube Data for Neutrino Point-Source Searches Years 2008-2018’. In: (Jan. 2021). DOI: 10.21234/CPKQ-K003. arXiv: 2101.09836 [astro-ph.HE].
- [86] M. G. Aartsen et al. ‘Measurement of Atmospheric Neutrino Oscillations at 6–56 GeV with IceCube DeepCore’. In: *Phys. Rev. Lett.* 120.7 (2018), p. 071801. DOI: 10.1103/PhysRevLett.120.071801. arXiv: 1707.07081 [hep-ex].

- [87] Lutz Köpke. ‘Improved Detection of Supernovae with the IceCube Observatory’. In: *J. Phys. Conf. Ser.* 1029.1 (2018), p. 012001. DOI: 10.1088/1742-6596/1029/1/012001. arXiv: 1704.03823 [astro-ph.HE].
- [88] M. G. Aartsen et al. ‘Search for neutrinos from decaying dark matter with IceCube’. In: *Eur. Phys. J. C* 78.10 (2018), p. 831. DOI: 10.1140/epjc/s10052-018-6273-3. arXiv: 1804.03848 [astro-ph.HE].
- [89] Anna Pollmann. ‘Searches for magnetic monopoles with IceCube’. In: *EPJ Web Conf.* 168 (2018). Ed. by B. Gwak et al., p. 04010. DOI: 10.1051/epjconf/201816804010.
- [90] J.V. Jelley. ‘The feasibility of detecting neutrinos of cosmic origin by radio frequency Cherenkov radiation in Antarctic ice’. In: *Astroparticle Physics* 5.3 (1996), pp. 255–261. ISSN: 0927-6505. DOI: [https://doi.org/10.1016/0927-6505\(96\)00026-6](https://doi.org/10.1016/0927-6505(96)00026-6). URL: <https://www.sciencedirect.com/science/article/pii/0927650596000266>.
- [91] R. E. Mikkelsen et al. ‘Characteristics of Cherenkov radiation in naturally occurring ice’. In: *Phys. Rev. D* 93 (5 Mar. 2016), p. 053006. DOI: 10.1103/PhysRevD.93.053006. URL: <https://link.aps.org/doi/10.1103/PhysRevD.93.053006>.
- [92] Wing Yan Ma. ‘Physics Potential of the IceCube Upgrade’. In: *J. Phys. Conf. Ser.* 1468.1 (2020). Ed. by Masayuki Nakahata, p. 012169. DOI: 10.1088/1742-6596/1468/1/012169.
- [93] Christopher Henrik V. Wiebusch. ‘The Detection of faint light in deep underwater neutrino telescopes’. Ph.D thesis. RWTH Aachen, 1995, p. 93. URL: <https://web.physik.rwth-aachen.de/~wiebusch/Publications/Various/phd.pdf> (visited on 15/04/2021).
- [94] MG Aartsen, R Abbasi et al. ‘Energy reconstruction methods in the IceCube neutrino telescope’. eng. In: *JOURNAL OF INSTRUMENTATION* 9 (2014), p. 36. ISSN: 1748-0221. URL: <http://dx.doi.org/10.1088/1748-0221/9/03/P03009>.
- [95] J. Ahrens et al. ‘Muon track reconstruction and data selection techniques in AMANDA’. In: *Nucl. Instrum. Meth. A* 524 (2004), pp. 169–194. DOI: 10.1016/j.nima.2004.01.065. arXiv: astro-ph/0407044.
- [96] Anatoli Fedynitch et al. *Calculation of conventional and prompt lepton fluxes at very high energy*. 2015. arXiv: 1503.00544 [hep-ph].
- [97] Felix Riehn et al. ‘The hadronic interaction model SIBYLL 2.3c and Feynman scaling’. In: *PoS ICRC2017* (2018), p. 301. DOI: 10.22323/1.301.0301. arXiv: 1709.07227 [hep-ph].
- [98] T. Pierog et al. ‘EPOS LHC: Test of collective hadronization with data measured at the CERN Large Hadron Collider’. In: *Phys. Rev. C* 92.3 (2015), p. 034906. DOI: 10.1103/PhysRevC.92.034906. arXiv: 1306.0121 [hep-ph].

- [99] Sergey Ostapchenko. ‘Monte Carlo treatment of hadronic interactions in enhanced Pomeron scheme: I. QGSJET-II model’. In: *Phys. Rev. D* 83 (2011), p. 014018. DOI: 10.1103/PhysRevD.83.014018. arXiv: 1010.1869 [hep-ph].
- [100] Stefan Roesler, Ralph Engel and Johannes Ranft. ‘The Monte Carlo event generator DPMJET-III’. In: *International Conference on Advanced Monte Carlo for Radiation Physics, Particle Transport Simulation and Applications (MC 2000)*. Dec. 2000. DOI: 10.1007/978-3-642-18211-2_166. arXiv: hep-ph/0012252.
- [101] Thomas K. Gaisser, Todor Stanev and Serap Tilav. ‘Cosmic Ray Energy Spectrum from Measurements of Air Showers’. In: *Front. Phys. (Beijing)* 8 (2013), pp. 748–758. DOI: 10.1007/s11467-013-0319-7. arXiv: 1303.3565 [astro-ph.HE].
- [102] J.-H. Koehne et al. ‘PROPOSAL: A tool for propagation of charged leptons’. In: *Computer Physics Communications* 184.9 (2013), pp. 2070–2090. ISSN: 0010-4655. DOI: <https://doi.org/10.1016/j.cpc.2013.04.001>. URL: <https://www.sciencedirect.com/science/article/pii/S0010465513001355>.
- [103] Kopper Claudio. *CLSim -Photon Propagation*. 2019. URL: <https://github.com/claudiok/clsim> (visited on 18/06/2020).
- [104] Christian Haack. ‘Observation of high-energy neutrinos from the galaxy and beyond’. PhD thesis. RWTH Aachen U., 2020. DOI: 10.18154/RWTH-2020-07059. URL: <https://publications.rwth-aachen.de/record/793612/files/793612.pdf> (visited on 16/04/2021).
- [105] Dirk Pandel. ‘Bestimmung von Wasser-und Detektorparametern und Rekonstruktion von Myonen bis 100 TeV mit dem Baikal-Neutrino teleskop NT-72’. In: *Humboldt-Universitaet Berlin* (1996).
- [106] Kai Schatto. ‘Stacked searches for high-energy neutrinos from blazars with IceCube’. PhD thesis. Mainz U., June 2014.
- [107] R. Abbasi et al. ‘An improved method for measuring muon energy using the truncated mean of dE/dx ’. In: *Nucl. Instrum. Meth. A* 703 (2013), pp. 190–198. DOI: 10.1016/j.nima.2012.11.081. arXiv: 1208.3430 [physics.data-an].
- [108] M.G. Aartsen et al. ‘Characterization of the atmospheric muon flux in IceCube’. In: *Astroparticle Physics* 78 (May 2016), pp. 1–27. ISSN: 0927-6505. DOI: 10.1016/j.astropartphys.2016.01.006. URL: <http://dx.doi.org/10.1016/j.astropartphys.2016.01.006>.
- [109] Jöran Stettner. ‘Measurement of the energy spectrum of astrophysical muon-neutrinos with the IceCube Observatory’. PhD thesis. RWTH Aachen U., 2021. DOI: 10.18154/RWTH-2021-01139.
- [110] Leif Rädcl. ‘Measurement of High-Energy Muon Neutrinos with the IceCube Neutrino Observatory’. PhD thesis. RWTH Aachen U., 2017. DOI: 10.18154/RWTH-2017-10054.

- [111] Sebastian Josef Schoenen. 'Discovery and characterization of a diffuse astrophysical muon neutrino flux with the iceCube neutrino observatory'. PhD thesis. RWTH Aachen U., 2017. DOI: 10.18154/RWTH-2017-06715.
- [112] Theo Glauch. 'The Origin of High-Energy Cosmic Particles: IceCube Neutrinos and the Blazar Case'. PhD thesis. Munich, Tech. U., 2021.
- [113] M. G. Aartsen et al. 'IceCube-Gen2: the window to the extreme Universe'. In: *J. Phys. G* 48.6 (2021), p. 060501. DOI: 10.1088/1361-6471/abbd48. arXiv: 2008.04323 [astro-ph.HE].
- [114] Matteo Agostini et al. 'The Pacific Ocean Neutrino Experiment'. In: *Nature Astron.* 4.10 (2020), pp. 913–915. DOI: 10.1038/s41550-020-1182-4. arXiv: 2005.09493 [astro-ph.HE].
- [115] S. Adrian-Martinez et al. 'Letter of intent for KM3NeT 2.0'. In: *J. Phys. G* 43.8 (2016), p. 084001. DOI: 10.1088/0954-3899/43/8/084001. arXiv: 1601.07459 [astro-ph.IM].
- [116] A. V. Avrorin et al. 'Baikal-GVD Experiment'. In: *Phys. Atom. Nucl.* 83.6 (2020), pp. 916–921. DOI: 10.1134/S1063778820060046.